

FEATURE ARTICLE

Spectral Properties and Relaxation Dynamics of Surface Plasmon Electronic Oscillations in Gold and Silver Nanodots and Nanorods

Stephan Link and Mostafa A. El-Sayed*

*Laser Dynamics Laboratory, School of Chemistry and Biochemistry, Georgia Institute of Technology, Atlanta, Georgia 30332-0400**Received: June 1, 1999; In Final Form: August 16, 1999*

The field of nanoparticle research has drawn much attention in the past decade as a result of the search for new materials. Size confinement results in new electronic and optical properties, possibly suitable for many electronic and optoelectronic applications. A characteristic feature of noble metal nanoparticles is the strong color of their colloidal solutions, which is caused by the surface plasmon absorption. This article describes our studies of the properties of the surface plasmon absorption in metal nanoparticles that range in size between 10 and 100 nm. The effects of size, shape, and composition on the plasmon absorption maximum and its bandwidth are discussed. Furthermore, the optical response of the surface plasmon absorption due to excitation with femtosecond laser pulses allowed us to follow the electron dynamics (electron–electron and electron–phonon scattering) in these metal nanoparticles. It is found that the electron–phonon relaxation processes in nanoparticles, which are smaller than the electron mean free path, are independent of their size or shape. Intense laser heating of the electrons in these particles is also found to cause a shape transformation (photoisomerization of the rods into spheres or fragmentation), which depends on the laser pulse energy and pulse width.

1. Introduction

As a consequence of reducing the size and the dimensionality of a material, its electronic properties change drastically as the density of states and the spatial length scale of the electronic motion are reduced with decreasing size.^{1–6} The energy eigenstates are now determined by the system's boundaries, and therefore, surface effects become very important.^{1–4,7} A transition from the bulk band structure to individual localized energy levels occurs in clusters of subnanometer to nanometer size, and the detection of quantum size effects has been of great interest to scientists in the search for novel materials with exciting new properties.^{5,8–10} Possible future applications of nanoparticles include the areas of ultrafast data communication and optical data storage,^{4,7,11} solar energy conversion,¹² and the use of metallic nanoparticles as catalysts because of their high surface-to-volume ratios.⁴

Metallic nanoparticles have fascinated scientists because of their colorful colloidal solutions long before semiconductors and their applications became an integral part of modern technology. Gold nanoparticles were used as a pigment of ruby-colored stained glass dating back to the 17th century.¹³ Faraday¹⁴ recognized that the red color is due to metallic gold in colloidal form, and Mie¹⁵ was the first to explain this phenomenon theoretically in 1908 by solving Maxwell's equation for the absorption and scattering of electromagnetic radiation by spherical particles. His theory has found wide applicability since then because it allows the calculation of the particle extinction spectra, as long as the material dielectric function is known and the size is smaller than the wavelength of the light.^{16–20}

The physical origin of the light absorption by metallic nanoparticles is the coherent oscillation of the conduction band

electrons induced by the interacting electromagnetic field.²¹ These resonances are known as surface plasmons and are indeed a small particle effect, since they are absent in the individual atoms as well as in the bulk.^{16–18,21} However, the size dependence of the surface plasmon absorption is not as easily explained as in the case of semiconductor nanoparticles,²¹ where a shift in the HOMO and LUMO results in a larger band gap and a blue shift of the absorption onset with decreasing size. This article reviews the size and shape dependence of the optical absorption spectra of mainly gold nanoparticles in colloidal solution. It also gives the results of the femtosecond dynamics of the electrons involved in the dephasing and relaxation of these plasmon oscillations.

2. Spectral Properties of Metallic Nanoparticles

2.1. Size Dependence of the Plasmon Absorption. The total extinction coefficient of small metallic particles is given in Mie's theory as the summation over all electric and magnetic multipole oscillations contributing to the absorption and scattering of the interacting electromagnetic field.^{15–18,21} For nanoparticles much smaller than the wavelength of the absorbing light (about 25 nm for gold particles) only the dipole term is assumed to contribute to the absorption (dipole approximation²¹). In the quasi-static regime the extinction coefficient κ for N particles of volume V is then given by the following equation.¹⁶

$$\kappa = \frac{18\pi NV\epsilon_m^{3/2}}{\lambda} \frac{\epsilon_2}{[\epsilon_1 + 2\epsilon_m]^2 + \epsilon_2^2} \quad (1)$$

λ is wavelength of the absorbing radiation and ϵ_m the dielectric

constant of the surrounding medium (assumed to be frequency-independent). ϵ_1 and ϵ_2 represent the real and imaginary parts of the material dielectric function, respectively ($\epsilon(\omega) = \epsilon_1(\omega) + i\epsilon_2(\omega)$, where ω is the angular frequency of the light). The absorbance A of a colloidal solution containing N particles in an optical cell with a path length L is $A = (\kappa/\ln 10)L$.

The resonance condition for the plasmon absorption is roughly fulfilled when $\epsilon_1(\omega) = -2\epsilon_m$ if ϵ_2 is small or weakly²¹ dependent on ω . The plasmon bandwidth mainly depends on $\epsilon_2(\omega)$. According to eq 1, the plasmon absorption is size-independent within the dipole approximation. However, experimentally a size effect on the surface plasmon absorption is observed as the plasmon bandwidth increases with decreasing particle size. It is in fact well established that the bandwidth is inversely proportional to the radius r of the particle for sizes smaller than about 20 nm.^{21,22–24}

Since Mie's theory has found wide applicability and has generally been successful in explaining optical absorption spectra of metallic nanoparticles,^{16–21} a size dependence for the quasi-static regime is introduced in eq 1 by assuming a size-dependent material dielectric function $\epsilon(\omega, R)$.^{21,24,25} The dielectric function can be written as a combination of an interband term $\epsilon_{IB}(\omega)$, accounting for the response of the d electrons, and a Drude term $\epsilon_D(\omega)$ considering the free conduction electrons only ($\epsilon(\omega) = \epsilon_{IB}(\omega) + \epsilon_D(\omega)$).^{26,27} The latter is given within the free electron model by the following expression.²⁶

$$\epsilon_D(\omega) = 1 - \frac{\omega_p^2}{\omega^2 + i\gamma\omega} \quad (2)$$

where $\omega_p^2 = [ne^2/(\epsilon_0 m_{\text{eff}})]$ is the bulk plasmon frequency expressed in terms of the free electron density n , the electron charge e , the vacuum permittivity ϵ_0 , and the electron effective mass m_{eff} ; γ is a phenomenological damping constant and equals the plasmon bandwidth Γ for the case of a perfect free electron gas in the limit²¹ of $\gamma \ll \omega$. The damping constant γ is related to the lifetimes of all electron scattering processes in the bulk material that are mainly due to electron–electron, electron–phonon, and electron–defect scattering. For a small particle, electron–surface scattering also becomes important, since the mean free path of the conduction electrons, typically in the range of tens of nanometers in noble metals, is limited because of the particle's boundaries. γ therefore becomes a function of the particle radius r .^{22,23}

$$\gamma(r) = \gamma_0 + \frac{Av_F}{r} \quad (3)$$

where γ_0 is the bulk damping constant, v_F is the velocity of the electrons at the Fermi energy, and A is a theory-dependent parameter that includes details of the scattering process (e.g., isotropic or diffuse scattering^{21,24}).

Kreibig first introduced this classical picture of the limitation of the electron mean free path and found good agreement with experimental results.²² An early quantum mechanical model developed by Kawabata and Kubo²⁸ also predicts a $1/r$ dependence of the plasmon bandwidth. However, their model does not treat the surface as a scatterer for the electrons; rather the surface determines the energy of the eigenstates of the system. Another more recent quantum mechanical model considers the adsorbed molecules on the nanoparticle surface.²⁹ It is suggested that the surface plasmon energy is transferred into excitation modes of the surface metal–adsorbate complex (chemical interface damping). Many more theories exist,^{21,24,30–33}

which all find a $1/r$ dependence, reflecting the importance of the ratio between the surface area and the volume. However, the slope parameter A (on the order of 1) depends on the theory.²⁴ Since the size dependence of the plasmon absorption in the quasi-static regime is introduced by assuming a size-dependent material dielectric function $\epsilon(\omega, R)$, the related changes in the optical absorption spectra are referred to as intrinsic size effects.²¹

For larger nanoparticles (>25 nm for gold particles) the extinction coefficient explicitly depends on the nanoparticle size as the higher order terms contribute, which are functions^{16–18} of r . For these large particles the plasmon bandwidth increases with increasing size as the wavelength λ of the interacting light becomes comparable to the dimension of the nanoparticle. This leads to an inhomogeneous polarization of the nanoparticle by the electromagnetic field. The broadening of the plasmon band is then usually ascribed to retardation effects.²¹ The increased line width is also caused by the excitation of different multipole modes, which peak at different energies.^{16–18} This behavior is referred to as an extrinsic size effect because the size dependence enters through the full expression of Mie's theory.²¹

Figure 1a shows the absorption spectra of different size gold nanoparticles with diameters of 9, 22, 48, and 99 nm.³⁴ They were prepared by chemical reduction of gold ions with sodium citrate in aqueous solution.^{35–37} The plasmon absorption is clearly visible, and its width follows the predicted behavior. For the size region of the quasi-static limit, intrinsic size effects dominate and the width increases with decreasing size. For the larger particles the plasmon bandwidth also increases because of extrinsic size effects. This relationship between the plasmon bandwidth and the particle radius r is also plotted in Figure 1b, including an additional sample of colloidal gold nanoparticles with a diameter of 15 nm.

The experimentally determined molar absorption coefficient κ' for the same series of gold nanoparticles determined at their respective plasmon absorption maxima is plotted against the nanoparticle volume V in Figure 1c. The molar absorption coefficient κ' is related to the measured absorbance A by $A = \kappa'[N]L$ where $[N]$ stands for the molar concentration of gold nanoparticles and L is the cell path length. $[N]$ is easily determined from the number of moles of gold ions before the reduction with sodium citrate, assuming that all the gold ions are reduced and form nanoparticles. The size of the nanoparticles, as determined from the magnified transmission electron microscopy (TEM) images, and the density of bulk fcc gold (59 atoms/nm³)²⁷ then gives the number of moles of gold nanoparticles in solution, which is in the range 10^{-8} – 10^{-9} M for 20 nm particles. The straight line in Figure 1c is a linear fit of the data points, illustrating that the molar absorption coefficient depends on the particle volume in a linear fashion. This is in agreement with Mie theory, which also predicts a linear relationship (eq 1). Note that the higher order terms that are not included in eq 1 have the same constant prefactor also yielding a linear dependence.^{16–18} More interesting about Figure 1c is, however, the magnitude of the molar absorption coefficient, which is several orders of magnitude larger than organic dye molecules (10^5 – 10^6 M⁻¹ cm⁻¹)³⁸ even for the smallest nanoparticles in Figure 1c. The molar absorption coefficient can alternatively be expressed in units of an absorption cross section (nm²) of an individual nanoparticle. This leads to a value for the absorption cross section of roughly 50% of the actual particle cross sectional area.

TEM images of the (a) 99 nm, (b) 48 nm, and (c) 15 nm gold nanoparticles after evaporation of the solvent (water) on a

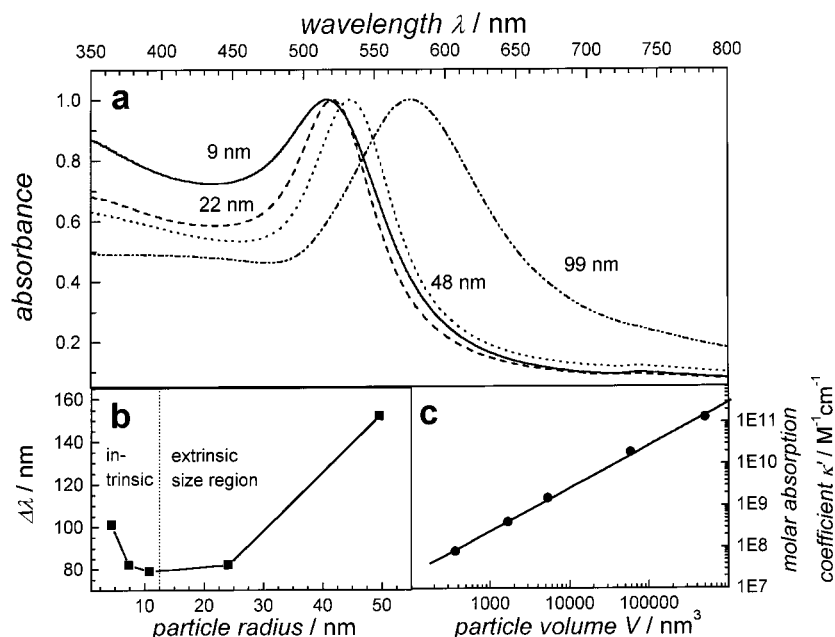


Figure 1. Size effects on the surface plasmon absorption of spherical gold nanoparticles. The UV-vis absorption spectra of colloidal solutions of gold nanoparticles with diameters varying between 9 and 99 nm show that the absorption maximum red-shifts with increasing particle size in part a, while the plasmon bandwidth follows the behavior illustrated in part b. The bandwidth increases with decreasing nanoparticle radius in the intrinsic size region and also with increasing radius in the extrinsic size region as predicted by theory. In part c the extinction coefficients of these gold nanoparticles at their respective plasmon absorption maxima are plotted against their volume on a double logarithmic scale. The solid line is a linear fit of the data points, illustrating that a linear dependence is observed, in agreement with the Mie theory (see eq 1).

carbon-covered copper grid taken at a magnification of 100 000 are given in Figure 2. The statistical size distributions are given in parts d–f of Figure 2. A standard deviation of $\sim 10\%$ is found for each sample, demonstrating that the observed size effects described above are not obscured by a varying size distribution. Furthermore, assuming a homogeneous size distribution, a dephasing time (T_2) of the coherent surface plasmon oscillation of 3.9 fs is calculated for the 15 nm particles.³⁴ The weak temperature dependence of the plasmon bandwidth also suggests that the dominant electronic dephasing mechanism involves electron–electron interactions rather than electron–phonon coupling.³⁴ This dephasing time is consistent with the results obtained by nonlinear studies using degenerate four-wave mixing (DFWM), which measures the macroscopic third-order susceptibility $\chi^{(3)}$ of colloidal gold solutions.^{39–43} Extremely fast dephasing times on the order of tens of femtoseconds have been deduced from these experiments as well.

So far only the size dependence of the plasmon bandwidth has been discussed. However, the absorption maximum of the surface plasmon oscillation also depends on the nanoparticle size.^{21,24} In the extrinsic size region the peak position shifts to longer wavelengths or correspondingly to lower energies as higher order multipole terms increasingly dominate.^{16–18} The situation is more complicated for smaller nanoparticles for which intrinsic size effects should dominate. Experimentally, both a blue shift and a red shift of the plasmon maximum have been found with decreasing size.²¹ Furthermore, the magnitude of the wavelength shift in the absorption maximum for nanoparticles in the intrinsic size region is small compared to the total line width of the plasmon resonance. The maxima of the plasmon absorption for the colloidal solutions shown in Figure 1b are 517, 520, and 521 nm for the 9, 15, and 22 nm nanoparticles, respectively. (The 48 and 99 nm particles falling in the extrinsic size region show absorption maxima at 533 and 575 nm.) The fact that a variety of theoretical approaches considering different small particle effects (e.g., changes of the band structure, environmental changes, or the “spill out” of the

conduction electrons) reach contradicting conclusions for the dependence of the plasmon band maximum on the nanoparticle size adds further confusion.²¹ The peak position of the surface plasmon oscillation is, therefore, usually not as well suited for a discussion of a size effect within the quasi-static regime.

2.2. Nanoparticle Alloy Formation and Its Effect on the Plasmon Absorption. While the peak position of the surface plasmon absorption of spherical gold nanoparticles is only weakly size-dependent, it varies strongly as a function of the composition for gold–silver alloy nanoparticles.^{44–48} This is illustrated in Figure 3a, which gives the absorption spectra of pure gold and gold–silver alloy nanoparticles. The alloy nanoparticles were produced by a simple co-reduction of gold and silver ions by sodium citrate.⁴⁸ Their compositions expressed in terms of the gold mole fractions x_{Au} are 0.8, 0.54, and 0.27. The maximum of the plasmon absorption clearly blue-shifts with decreasing gold mole fraction. This is also shown in Figure 3b where the plasmon maximum λ_{max} is plotted as a function of the gold mole fraction x_{Au} . A linear relationship is found experimentally, as illustrated by the dotted line in Figure 3b.^{48–50} This dependence of the plasmon band maximum on the alloy composition makes this system easily tunable for optical applications requiring a certain absorption spectrum.

The gold–silver alloy nanoparticle shape is found to be nearly spherical, and the mean particle diameter was determined to be 18 nm from TEM studies. The formation of homogeneous alloy nanoparticles by this method was confirmed by high-resolution TEM (HRTEM)⁴⁸ and energy dispersive spectrometry. Gold–silver alloy nanoparticles have also been synthesized in 2-butanol by evaporation and condensation of the alloys⁴⁴ and have been grown in photosensitive glasses.⁴⁵ Furthermore, it has been reported⁴⁷ that gold–silver bimetallic clusters can be prepared by radiolysis of the mixed metal salt solutions. The composition of the bimetallic clusters changes from a bilayered core–shell structure to an alloy with an increase of the radiolysis dose rate. This is explained⁴⁷ in terms of a less important reverse electron transfer process from reduced silver atoms (less noble metal)

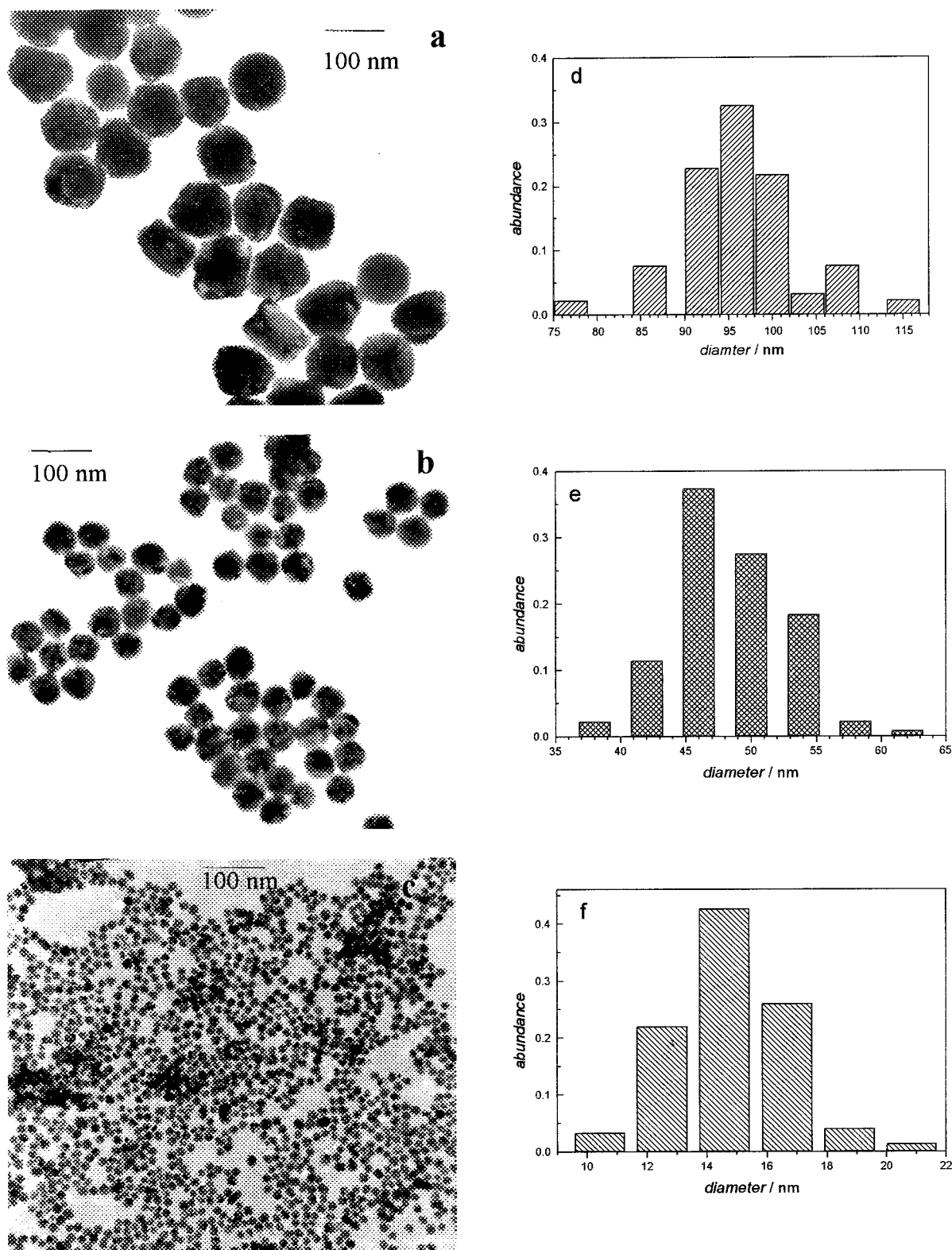


Figure 2. TEM images of spherical gold nanoparticles with average diameters of 99, 48, and 15 nm are given in parts a–c, respectively. Their size distributions as determined by counting at least 300 particles are shown in parts d–f. The TEM images correspond to the samples studied in Figure 1, and because of their nearly constant size distribution, a direct comparison of their optical properties is justified.

to gold ions (more noble metal) relative to the rate of direct reduction of both ions by radiolytic species. Of technological interest is the admixture of platinum and palladium to gold, since pure gold nanoparticles have only a low catalytic activity.^{51–54}

While the alloy formation of two metals for nanometer size particles and the corresponding phase diagram are of interest

for the material scientists, the linear relationship between the plasmon absorption maximum and the particle composition deserves some additional comments here. Combining the resonance condition for the plasmon absorption in the dipole approximation ($\epsilon_1(\omega) = -2\epsilon_m$) with the expression for the free electron contribution to the real part of the dielectric function $\epsilon_{1D}(\omega)$ yields the following approximation for the maximum of

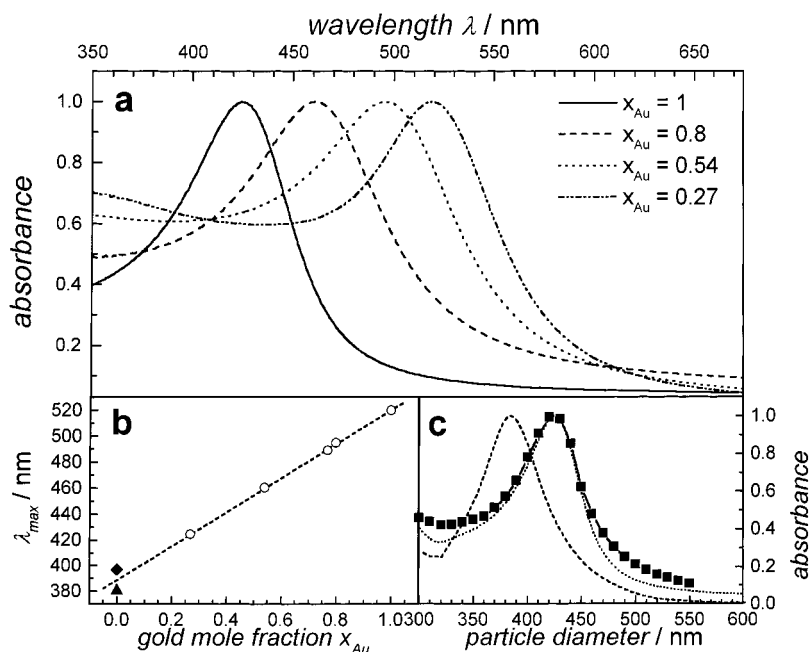


Figure 3. Effect of gold–silver alloy formation on the surface plasmon absorption. Part a shows the UV–vis absorption spectra of spherical gold–silver alloy nanoparticles of varying composition. The gold mole fraction x_{Au} varies between 1 and 0.27. The plasmon absorption maximum blue-shifts with decreasing x_{Au} . This fact is further illustrated in part b where the plasmon band maximum is plotted as a function of the gold mole fraction x_{Au} . The open circles correspond to experimental data from ref 47, while the value of the plasmon maximum of pure silver nanoparticles is taken from refs 48 and 49. The dashed line is a linear fit to the data points, demonstrating that the dependence of the plasmon band maximum on x_{Au} is best described by a linear relationship. Part c shows the experimental UV–vis absorption spectrum of gold–silver alloy nanoparticles ($x_{\text{Au}} = 0.27$, dotted line) and two calculated absorption spectra using the Mie equation and different values for the dielectric function. The dashed line gives the spectrum calculated by using a mole-fraction-weighted dielectric function of gold and silver. Better agreement between theory and experiment is found if the experimental dielectric function obtained from an alloy thin film with a similar composition ($x_{\text{Au}} = 0.28$) is used in the Mie equation (squares, solid line).

the plasmon absorption.²¹

$$\omega_{\text{max}} = \left(\frac{ne^2}{\epsilon_0 m_{\text{eff}} (1 + \epsilon_m)} \right)^{1/2} \quad (4)$$

This free electron approximation cannot, however, explain the blue shift of the surface plasmon absorption because the electron density n and effective mass m_{eff} are very similar for gold and silver.^{26,55} In fact, eq 4 should not be applied to gold and silver nanoparticles because the surface plasmon oscillation in these particles is a hybrid resonance resulting from the excitation of the conduction as well as the d-band electrons.²¹

It has been proposed^{20,46} that the dielectric function of the alloy particles can be treated as a combination of the dielectric function of gold and silver in the form $\epsilon(\alpha) = (1 - \alpha)\epsilon_{\text{Au}} + \alpha\epsilon_{\text{Ag}}$. The dipolar resonance has been calculated for alloy nanoparticles with a gold mole fraction of 0.27 using eq 1 and dielectric data taken from ref 56 and is shown in Figure 3c (dashed line) together with the experimental absorption spectrum (dotted line). Obviously, this assumption cannot reproduce the experimental spectrum, since the absorption maximum is shifted by 35 nm to longer wavelengths. However, if the dielectric function measured on a thin gold–silver alloy film with a composition of 0.28⁵⁷ is used, excellent agreement can be achieved as illustrated by the third spectrum in Figure 3c (squares and solid line). This result leads to two important conclusions. (1) The classification as alloy nanoparticles is indeed justified. Furthermore, the band structure and all resulting optical properties of gold–silver alloys cannot be viewed as a simple linear combination of the electronic structures of pure gold and silver. (2) These simple calculations show how important it is to use the correct expression of the material

dielectric function. This has been stressed by Kreibig who showed that a choice of an arbitrary set of hypothetical dielectric functions can even result in a multipeak structure.²¹ On the hand, the same author also demonstrated how the dielectric function of a nanoparticle can be computed from its optical absorption spectrum by Kramers–Kronig analysis.²³

The position and shape of the plasmon absorption of spherical metallic nanoparticles depend not only on their composition and, hence, on the correct form of the material dielectric function, but also on the dielectric function of the surrounding medium ϵ_m (see eq 1). Increasing ϵ_m leads to an increase in the plasmon band intensity and bandwidth as well as to a red shift of the plasmon band maximum.²¹ (The last effect is even more pronounced for the longitudinal mode of the surface plasmon oscillation in nanorods discussed in the next section.) Changing the surrounding medium to one with a higher dielectric constant and therefore enhancing the plasmon absorption is known as immersion spectroscopy.²¹ Furthermore, Henglein et al.^{1,2,58} have shown in a variety of experiments on silver colloids that adsorbed molecules on the particle surface cause a strong damping and broadening of the plasmon band. However, neither a change of the free electron density (charge-transfer processes) nor a change of the medium dielectric constant can account for the magnitude of the damping in a quantitative way.¹

The coupling of the surface plasmon oscillation with individual acceptor levels of molecules attached to the nanoparticle surface has recently been discussed as a possible quantitative explanation and is known as chemical interface damping (CID).^{29,59,60} On the basis of this theory, the energy of the adsorbate-induced resonance state, lying energetically above the Fermi level of the metal, has to match the surface plasmon energy in order to efficiently dampen the free electron oscilla-

tion. It is therefore an important difference if the adsorbed molecules are bound to the surface atoms by physisorption or chemisorption processes. An elegant experiment to test this theory was carried out by Hoevel et al.⁵⁹ in which the optical absorption spectra of the same 2 nm silver clusters were first measured in the gas phase and then deposited on a SiO₂ substrate and finally embedded in a SiO₂ matrix. Their results support the concept of chemical interface damping.

Although not a new research field in the area of metal cluster (nanoparticle) spectroscopy, the origin of the strong damping of the surface plasmon oscillation by different chemical environments is still of current interest. With the fast growing area of nanoparticles for possible future applications, the stabilization of the nanoparticles and their incorporation into solid matrices for actual devices requires an understanding of the interactions at the nanoparticle–surrounding medium interface and their influence on the optical properties of the whole system. The use of the plasmon resonance as a chemical sensor has even been proposed.⁶⁰

2.3. Shape Dependence of the Plasmon Absorption. A much more drastic effect on the surface plasmon absorption is found if the nanoparticle shape is changed.^{16,21,61–65} For gold nanorods, the plasmon absorption splits into two bands^{62–65} corresponding to the oscillation of the free electrons along and perpendicular to the long axis of the rods.¹⁶ The transverse mode shows a resonance at about 520 nm, which is coincident with the plasmon band of spherical particles, while the resonance of the longitudinal mode is red-shifted and strongly depends on the nanorod aspect ratio R ;^{62–65} the aspect ratio is defined as the length of the rod divided by the width of the rod. An absorption spectrum of colloidal gold nanorods clearly showing the presence of the two absorption maxima is shown in Figure 4b. The corresponding TEM image of these nanorods with a mean aspect ratio of 4.1 is shown in Figure 4a. The average length and width of the gold nanorods are 44 and 11 nm, respectively. The gold nanorods were synthesized by an electrochemical method in the presence of organic surfactants forming protecting rod-shaped micelles around the gold nanorods.⁶²

The optical absorption spectrum of a collection of randomly orientated gold nanorods with aspect ratio R can be modeled by using an extension of Mie's theory.¹⁶ According to Gans,⁶¹ the extinction coefficient κ for N particles of volume V is given within the dipole approximation by the following equation.

$$\kappa = \frac{2\pi N V \epsilon_m^{3/2}}{3\lambda} \sum_j \frac{(1/P_j^2)\epsilon_2}{\left(\epsilon_1 + \frac{1 - P_j}{P_j}\epsilon_m\right)^2 + \epsilon_2^2} \quad (5)$$

P_j values are the depolarization factors for the three axes A , B , and C of the nanorod with $A > B = C$.

$$P_A = \frac{1 - e^2}{e^2} \left[\frac{1}{2e} \ln \left(\frac{1+e}{1-e} \right) - 1 \right] \quad (6)$$

$$P_B = P_C = \frac{1 - P_A}{2} \quad (7)$$

$$e = \sqrt{1 - \left(\frac{B}{A}\right)^2} = \sqrt{1 - \frac{1}{R^2}} \quad (8)$$

The absorption spectra of gold nanorods with varying aspect ratios were calculated with the measured dielectric function of

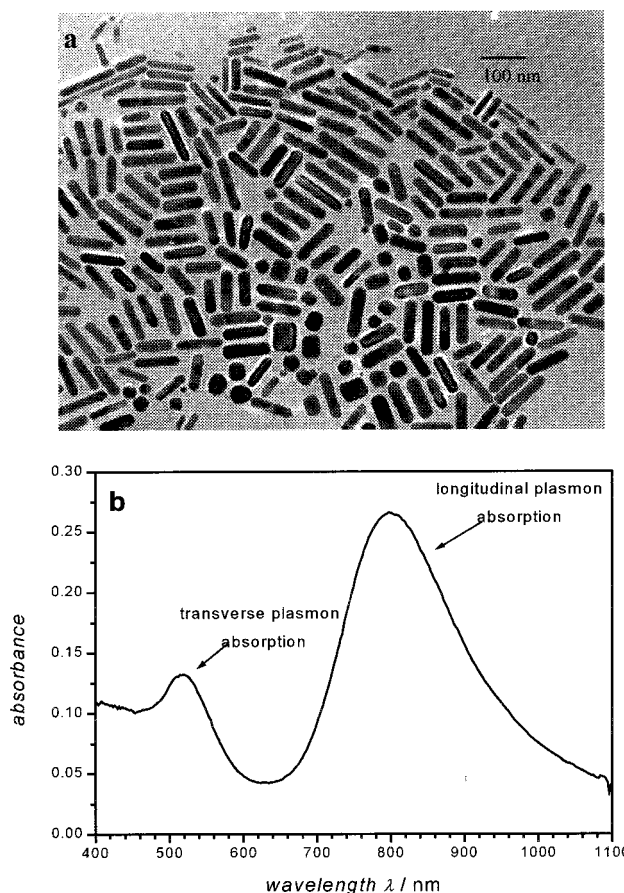


Figure 4. Gold nanoparticles of cylindrical shape and the effect on the optical absorption spectrum. Part a displays a TEM image of gold nanorods with an average aspect ratio of 4.1. Part b shows the corresponding UV–vis absorption spectrum of the colloidal gold nanorod solution. The absorption band at 520 nm is the transverse mode of the surface plasmon absorption, while the longitudinal mode absorbs around 800 nm for these rods with a 4.1 aspect ratio.

gold⁵⁶ using eqs 5–8⁶⁴ and are shown in Figure 5a. The medium dielectric constant was chosen to be a fixed value of 4. The maximum of the longitudinal plasmon band red-shifts 150 nm when the aspect ratio is increased from 2.6 to 3.6. Furthermore, the increase in the peak position of the longitudinal plasmon band with increasing nanorod aspect ratio follows a linear trend, which is illustrated in Figure 5b. The data points in Figure 5b correspond to the absorption maxima as determined from the calculated spectra in Figure 5a. The solid line is a plot of an equation derived⁶⁴ in order to predict the maximum of the longitudinal plasmon band λ_{\max} .

$$\begin{aligned} \lambda_{\max} &= 33.34\epsilon_m R - 46.31\epsilon_m + 472.31 \\ &= (33.34R - 46.31)\epsilon_m + 472.31 \end{aligned} \quad (9)$$

The good agreement between the points and the line in Figure 5b justify the simplifications made in the derivation of eq 9. Furthermore, from eq 9 it follows that the maximum of the longitudinal plasmon mode should also depend on the medium dielectric constant ϵ_m in a linear way; for a fixed aspect ratio, λ_{\max} red-shifts with increasing medium dielectric constant. The calculated dependence is shown in Figure 5c for $R = 3.3$. It should be pointed out again that a peak shift of about 150 nm is observed when the medium dielectric constant is increased by just 1.

Figure 6a now shows the experimental results for the dependence of the absorption maximum of the longitudinal

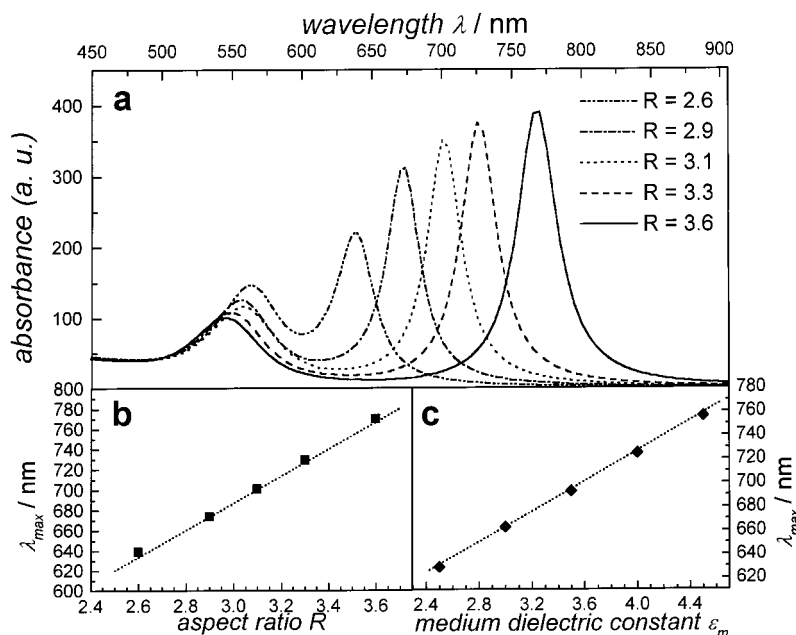


Figure 5. Simulation of the surface plasmon absorption for gold nanorods of different aspect ratio. Part a shows the calculated absorption spectra of gold nanorods with varying aspect ratios R using the theory developed by Gans (eq 5). The dependence of the maximum of the longitudinal plasmon absorption as a function of the gold nanorod aspect ratio R and the medium dielectric constant ϵ_m for a constant value of the other parameter are given in parts b and c, respectively. The data points are extracted from calculated spectra, while the dotted lines are obtained by using eq 9 for $\epsilon_m = 4$ (b) and $R = 3.3$ (c) (see text). Excellent agreement between the predicted data points using the full Gans expression and the simplified eq 9 is found.

plasmon resonance on the nanorod aspect ratio.⁶⁴ The solid line is a linear fit to the data points, which were obtained from the optical absorption spectra of several gold nanorod samples synthesized by varying the ratio of surfactant to cosurfactant molecules of the stabilizing micelles. A linear relationship similar to that in Figure 6a was also reported by Yu et al.⁶² for the nanorods prepared in the same way and is furthermore in agreement with studies of poly(vinylpyrrolidone)-stabilized gold nanorods in aqueous solution.⁶⁵

The fact that a linear dependence of the absorption maximum of the longitudinal resonance is found experimentally compares well with the theoretical predictions of Figure 5b. However, it is not possible to match the experimental results with eq 9 for a single value of the medium dielectric constant. Only if the medium dielectric constant becomes a function of the aspect ratio can this discrepancy be resolved. The medium dielectric constant ϵ_m needed to fit the experimental data increases with decreasing aspect ratio R as shown in Figure 6b. This occurs because the ratio of surfactant to cosurfactant molecules must be varied in order to prepare gold nanorods with different aspect ratios. In chemical terms, gold nanorods of varying length and therefore aspect ratio are encapsulated by micelles of different composition, which results in a different medium dielectric constant as experienced by the gold nanorods.⁶⁴

Gold nanorods with varying aspect ratios have also been synthesized by electrodeposition of the metal within the pores of anodically grown porous aluminum oxide membranes.^{65–70} The individual nanorods are well separated and aligned parallel to each other within the optically transparent aluminum oxide membrane. The optical properties of these composite materials have been studied extensively by Martin et al.^{66–70} as a function of pore diameter and gold nanorod aspect ratio. The optical absorption spectra show only one plasmon absorption band. However, since the spectra were measured with the electric field vector of the incident light wave pointing perpendicular to the long axis of the nanorods, the observed plasmon band should correspond to the transverse mode. The spectral position of the

absorption maximum confirms this conclusion. Furthermore, it was found experimentally by Martin et al.^{66–70} that the plasmon band maximum blue-shifts with increasing aspect ratio.

The observed blue shift of the plasmon band of gold nanorods in aluminum oxide membranes is in agreement with theoretical predictions. Maxwell–Garnett theory^{16,21} was applied^{71,72} to model the optical absorption spectra in this case. The Maxwell–Garnett theory is an effective medium theory with which the complex dielectric function of the composite material can be calculated as a function of frequency if the dielectric data of the metal and the host matrix are known.^{16,21} The composite dielectric function only depends on the volume fraction and shape of the metal particles.^{71,72} The absorption spectrum of a composite film can then be easily calculated with the known relationship between the complex dielectric function and the refractive index and absorption coefficient. A blue shift of the transverse mode of the surface plasmon absorption with increasing aspect ratio was also calculated for randomly orientated gold nanorods in solution by using eq 5⁶⁴ (see Figure 5a). However, for colloidal gold nanorods prepared by the electrochemical method the shift in the absorption maximum of the longitudinal resonance is a much more sensitive parameter when describing the optical properties as a function of nanorod aspect ratio.

A second red-shifted plasmon absorption is also found for nanoparticle aggregates. It has been shown theoretically and experimentally that aggregation of gold nanoparticles leads to another plasmon absorption at longer wavelengths when the individual nanoparticles are electronically coupled to each other.^{73–75} The oscillating electrons in one particle feel the electric field due to the oscillation of the free electrons in a second particle, which can lead to a collective plasmon oscillation of the aggregated system. The frequency and intensity of the latter depend on the degree of aggregation as well as the orientation of the individual particles within the aggregate.^{21,24,73–75} This interparticle coupling is certainly stronger than the coupling with the surrounding medium, and Mie's theory developed for

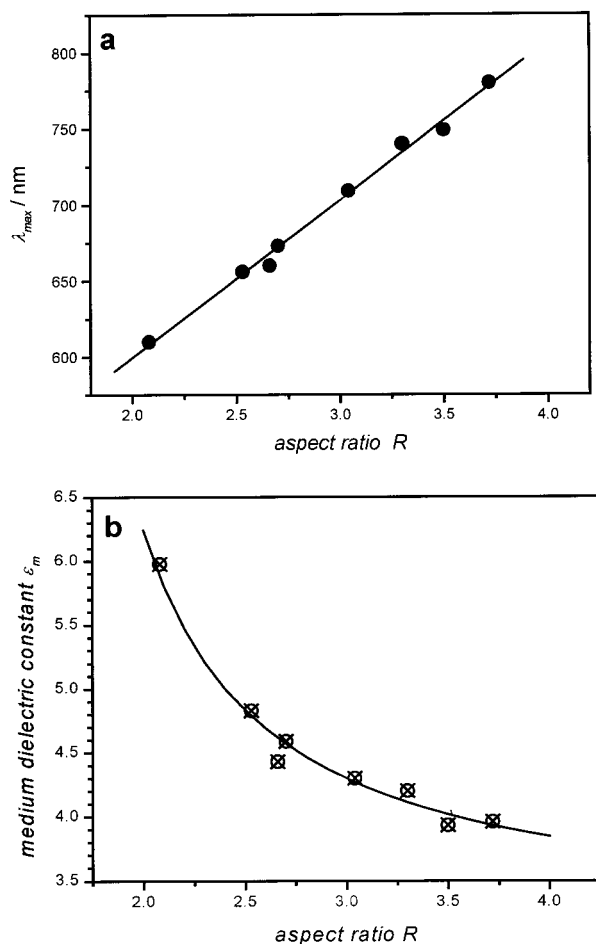


Figure 6. Comparison of the predictions made by the simulation in Figure 5 with experimental data. Part a shows the experimentally determined dependence of the longitudinal plasmon absorption maximum on the gold nanorod aspect ratio R . The solid line is a linear fit to the data points. Although a linear relationship between absorption maximum and aspect ratio is found, modeling of the experimental absorption spectra with a single value for the medium dielectric constant fails. Part b illustrates how the medium dielectric constant has to vary as a function of the aspect ratio in a nonlinear way in order to reproduce the experimental absorption maximum. The data points in part b correspond to the experimental points in part a, while the solid line gives the relationship used to calculate the line in part a.

very dilute solutions and isolated particles fails to describe the optical absorption spectrum. However, effective medium theories have been successfully applied to this problem.²¹

3. Nonradiative Relaxation Dynamics of the Surface Plasmon Oscillation

3.1. Femtosecond Dynamics in Metallic Nanoparticles. The dephasing of the coherent plasmon oscillation in metallic nanoparticles is related to the homogeneous plasmon absorption bandwidth and can be probed by steady-state absorption spectroscopy. On the other hand, time-resolved pump–probe transmission measurements monitor the optical response of the electrons after excitation with ultrashort laser pulses.^{76–95} The plasmon band absorption serves as a convenient and very sensitive tool for following the electron dynamics, such as electron–electron and electron–phonon scattering within the nanoparticle system. The pump pulse selectively excites the electrons, with the electron gas reaching temperatures of up to several thousand degrees kelvin depending on the pump fluence.^{77,84} Initially, a non-Fermi electron distribution is created

that thermalizes internally through electron–electron scattering. Subsequently, the electron gas cools externally by electron–phonon interactions until the temperatures of the electron gas and the lattice are equilibrated. Finally, phonon–phonon interactions with the surrounding medium lead to a complete relaxation of the initially absorbed photon energy.

The separation between electron and lattice heating is justified, since the electronic heat capacity is about 2 orders of magnitude smaller than the lattice heat capacity. This assumption forms the basis of the two-temperature model (TTM),⁹⁶ which has been widely used to explain results obtained on thin metal films.^{97–109} Time-resolved transmissivity and reflectivity^{97–107} as well as two-photon photoemission spectroscopy^{108–113} on thin metal films (thickness: 10–100 nm) has been used to study electron–electron and electron–phonon interactions. The results from these measurements can be directly related to the electron dynamics in metallic nanoparticle systems. These investigations are of great interest, since they are essential in addressing such fundamental questions as the thermal and electrical conductivity in metals, and are important for understanding the nature of superconductivity.

In the case of nanoparticles, the heating of the electron gas leads to spectral broadening of the surface plasmon absorption.^{76–84} This results in a transient bleach centered at the plasmon band maximum and two positive absorption wings at lower and higher energies in the difference spectrum.^{76,81} Femtosecond transient absorption spectra of 15 nm spherical gold nanoparticles recorded at different delay times between the excitation (pump) pulse and the white light probe pulse are shown in Figure 7a. The excitation wavelength in this experiment was 400 nm, produced by second harmonic generation of the fundamental of an amplified Ti:sapphire system (1 mJ output power at 1 kHz repetition rate and 100 fs pulse width). Physically, this transient behavior of the plasmon band broadening after laser excitation can also be understood as a faster dephasing time T_2 of the coherent plasmon oscillation compared to the unexcited (ground) state.^{80–82} At higher temperatures the occupation of higher electronic states leads to an increased electron scattering rate (Fermi liquid theory,¹¹⁴ see eq 12) and thus to an increased damping of the plasmon oscillation. Perner et al.⁸¹ found an increase in the plasmon bandwidth of gold nanoparticles embedded in a sol–gel matrix by 120 meV and calculated an average electron–electron scattering rate of $(10 \text{ fs})^{-1}$ for a hot electron distribution at 4000 K.⁸¹ The steady-state absorption of the colloidal gold nanoparticle solution is also displayed in Figure 7a in order to show that the bleach maximum coincides with the peak position of the plasmon absorption. The decay of the transient bleach monitored at the bleach maximum at 520 nm follows a biexponential behavior. The short time component of 3.1 ps is assigned to electron–phonon relaxation, while the long time component of 90 ps is due to phonon–phonon relaxation with the water molecules (see inset in Figure 7a).^{76–78} While the spectral position of the plasmon bleach is shifted for gold–silver alloy nanoparticles ($x_{\text{Au}} = 0.8$), the electron dynamics are similar to those of pure gold nanoparticles (Figure 7b) and allow one to have a tunable system for possible applications with an ultrafast response time.⁷⁸

Concluding this section, it is important to again emphasize the difference between energy relaxation after excitation with femtosecond laser pulses and the dephasing of the coherent plasmon oscillation. The decay of the transient negative absorption (bleach) signal is assigned to the cooling of the hot electron gas by inelastic collisions with the phonons of the lattice on

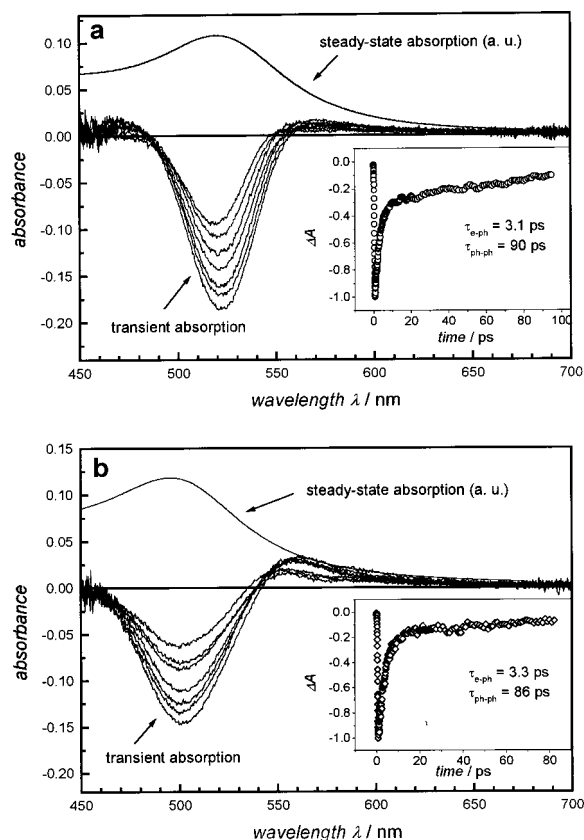


Figure 7. Independence of the electron–phonon and phonon–phonon relaxation times on the composition of gold and mixed gold–silver nanoparticles. Part a shows the transient absorption spectra of 15 nm spherical gold nanoparticles after excitation at 400 nm with 100 fs laser pulses recorded at different delay times. Also shown is the steady-state UV–vis absorption spectrum of the colloidal gold solution. The inset shows the decay of the transient bleach when the particles are monitored at the bleach maximum at 520 nm. Fitting of the decay curve gives electron–phonon and phonon–phonon relaxation times of 3.1 and 90 ps, respectively. Part b shows the transient absorption spectra and steady-state UV–vis absorption spectrum of 18 nm gold–silver alloy nanoparticles ($x_{\text{Au}} = 0.8$) after excitation at 400 nm with 100 fs laser pulses recorded at different delay times. The inset shows the decay of the transient bleach when the particles are monitored at the bleach maximum at 500 nm. Fitting of the decay curve gives electron–phonon and phonon–phonon relaxation times of 3.3 and 86 ps, respectively. These numbers are similar to those obtained in part a, indicating very similar electron dynamics in gold–silver alloy nanoparticles.

the picosecond time scale (energy relaxation, T_1), while the width of the plasmon band is caused by the loss of coherence of the free electron oscillation (pure dephasing, T_2). This last process involves both elastic and inelastic electron scattering processes, which are on the order of 10 fs as already discussed in section 2.1.

3.2. Pump Power Dependence of the Electron–Phonon Relaxation Dynamics. The time evolution of the electron and lattice temperatures T_e and T_l after excitation with a laser pulse can be described quantitatively by a set of coupled differential equations:^{101,102}

$$\frac{\delta T_e}{\delta t} = -\frac{g}{C_e}(T_e - T_l) + LP(t) \quad (10)$$

$$\frac{\delta T_l}{\delta t} = \frac{g}{C_l}(T_e - T_l) \quad (11)$$

C_e and C_l are the electronic and lattice heat capacities,

respectively, g is the electron–phonon coupling constant, and $LP(t)$ is the intensity profile of the exciting laser pulse as a function of time t . Since the electronic heat capacity depends on the electron temperature ($C_e \sim T_e$),^{26,27} the effective rate constant $g/C_e(T_e)$ for the thermal relaxation of the electron gas $\delta C_e/\delta T_e$ is also temperature-dependent and therefore decreases with increasing pump laser power. As a consequence, the experimentally measured electron–phonon relaxation time increases with increasing electron temperature and hence pump power.^{77,84} This is illustrated in Figure 8a, which shows four different kinetic traces of the plasmon bleach recovery for 15 nm spherical gold nanoparticles, monitored at 520 nm after excitation with 400 nm femtosecond laser pulses of different laser power. The measured lifetimes in order of increasing pump power are 1.5, 2.0, 3.3, and 3.6 ps at excitation laser powers of 50, 80, 100, and 160 nJ, respectively. The spot size of the laser beam was estimated to be roughly 125 μm , which leads to an electron temperature of approximately 2200 K for the lowest excitation power of 60 nJ and a corresponding rise in the lattice temperature of about 60 K if all the deposited laser power is transferred into lattice phonons.

A plot of the measured electron–phonon relaxation times τ_{e-ph} from Figure 8a against the pump power (normalized to the maximum laser power) is shown in Figure 8b. A linear fit of the data points yields a limiting decay time of 690 ± 100 fs for zero excitation power. The results obtained by exciting at 630 nm (circles and dotted line) are also included in Figure 8b and give a decay time of 830 ± 100 fs. With $g = C_e/\tau_{e-ph}$ in the low excitation limit and by use of the average of several measurements, an electron–phonon coupling constant of $(2.5 \pm 0.5) \times 10^{16} \text{ W m}^{-3} \text{ K}^{-1}$ is obtained, in agreement with results obtained on gold nanoparticles⁸⁴ as well as on bulk gold.⁹⁸

Since heat dissipation by electron diffusion is not important in nanoparticles compared to thin films^{101,102} (and was therefore omitted in eq 10), this power dependence of the electron–phonon relaxation could also be caused by the fact that phonon–phonon relaxation with the surrounding solvent is much slower than electron–phonon relaxation.⁷⁷ Thus, phonon–phonon relaxation, which is not included in eqs 10 and 11, becomes the rate-determining step. Since heat is not released to the solvent (or solid matrix), the lattice itself could heat the electrons, causing a longer decay of the measured transient bleach signal. In fact, with increasing pump power the magnitude of the offsets in the kinetic traces in Figure 8a increases. The offset was modeled with a 100 ps decay time representing the phonon–phonon interactions. The amplitude ratio of the long time component to the electron–phonon relaxation is displayed in Figure 8c.

Furthermore, the power dependence of the electron–phonon relaxation could also explain the slightly different results obtained for gold nanoparticles in solution or embedded in a solid matrix by several authors, although effects on the electron–phonon interaction resulting from different surrounding media cannot be excluded. Ahmadi et al.^{76,77} reported decay times of 2.5 and >50 ps for the electron–phonon and phonon–phonon relaxation times in 30 nm colloidal gold particles using excitation wavelengths of 380 and 600 nm. Hodak et al.^{83,84} performed a series of measurements at different powers for the electron–phonon relaxation of 11 nm gold particles, which showed that the measured relaxation times depend linearly on the laser power for the low excitation limit. Their experiments yielded a limiting decay time of 0.8 ps, similar to that seen in Figure 8. Perner et al.^{80–82} measured relaxation times of 4 and 200 ps for 30 nm gold particles embedded in a sol–gel matrix

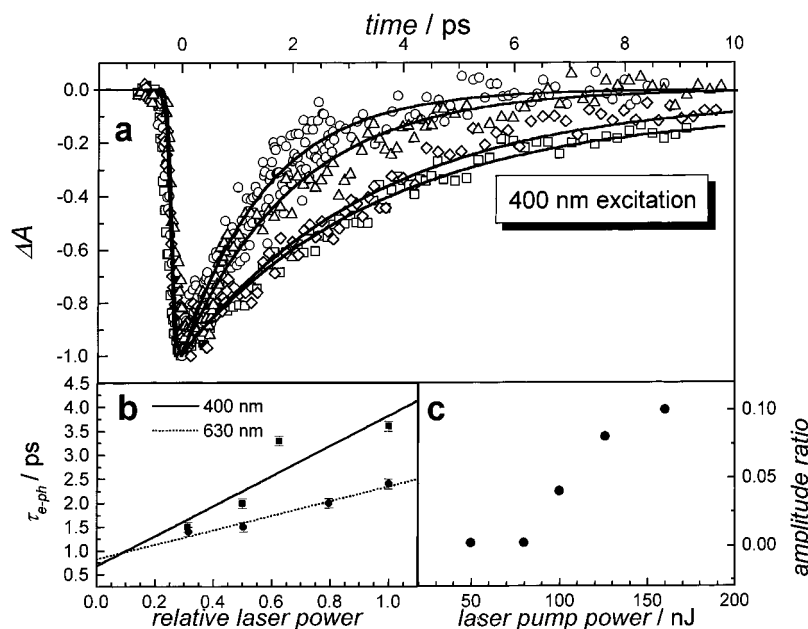


Figure 8. Power dependence of the electron–phonon relaxation time. Part a shows the results for 15 nm spherical gold nanoparticles after 400 nm excitation. The bleach recovery is monitored at the bleach maximum of 520 nm. The decay curves were fitted with lifetimes of 1.5, 2.0, 3.3, and 3.6 ps for excitation powers of 50, 80, 100, 160 nJ, respectively. Part b shows a plot of the electron–phonon relaxation times against the relative laser pump power. Extrapolation to zero laser power yields a decay time of 690 ± 100 fs for 400 nm excitation. The result for 630 nm excitation is also included, which gives a limiting decay time of 830 ± 100 fs. This result corresponds to an electron–phonon coupling constant of about $(2.5 \pm 0.5) \times 10^{16} \text{ W m}^{-3} \text{ K}^{-1}$. At high laser pump powers the bleach also shows a long time component as seen by the offset of the decay curves in part a. This corresponds to the phonon–phonon relaxation, which occurs on a time scale of 100 ps. The amplitude ratio of the phonon–phonon to the electron–phonon relaxation time increases with increasing laser power, as plotted in part c.

after excitation at 400 nm. Inouye et al.⁹³ measured gold nanoparticles with a diameter of 7.6 nm in a SiO_2 glass matrix and found decay times of 2.8 and 120 ps. Smith et al.^{88–90} on the other hand observed longer relaxation times of 7 and 400 ps for 15 nm gold nanoparticles in water when the nanoparticles are probed at 790 nm after excitation with 390 nm pulses having a much higher energy (several microjoules). They also reported a reduction of the decay times for electron–phonon interactions from 7 to 3.5 ps when the solvent was changed from water to cyclohexane. The relaxation dynamics of the excited electrons in a nanoshell of gold sulfide nanoparticles coated with an outer layer of gold were reported by Averitt et al.⁹⁵ They found a lifetime of 1.7 ps, which is very similar to the results for pure gold nanoparticles.

However, aggregation of gold nanoparticles and the interparticle coupling might also be of importance, as demonstrated by Feldstein et al.⁹² They prepared a series of thin films by wet chemistry techniques from 12 nm gold nanoparticles and studied their electronic relaxation dynamics. With increasing nanoparticle aggregation, corresponding to thicker films, the measured lifetimes for the electron–phonon relaxation increased from 1 to 3 ps. On the basis of their results, it can be concluded that the interparticle distances and the domain (or aggregate) sizes also influence the electron dynamics in (coupled) metallic nanoparticle systems.

Femtosecond studies of other metals include mainly silver. Roberti et al.⁸⁷ investigated 10 nm silver particles and found decay times of 2 and 40 ps when the particles are probed between 660 and 790 nm. Hodak et al.⁸⁴ found lifetimes of about 1 ps for 10 and 50 nm silver particles. A similar decay time of 0.7 ps was also obtained for 4 nm copper nanoparticles in a glass matrix by Tokizaki et al.⁹⁴ The similar lifetimes for the nanoparticles of the noble metals and especially the close agreement between the values for gold and silver obtained by the same authors can explain why the relaxation times do not

change upon alloy formation. The same optical density of the samples and the same excitation power were used for the gold and gold–silver alloy nanoparticles in parts a and b of Figure 7, and therefore, very similar time constants were obtained, in agreement with no change in the electron–phonon coupling in pure gold and silver nanoparticles.⁷⁸

3.3. Electron–Electron Thermalization in Metallic Nanoparticles. Several research groups have studied the hot electron dynamics in thin gold films using femtosecond transient transmissivity and reflectivity as well as time-resolved two-photon photoemission techniques and also reported slightly different electron–phonon relaxation times.^{97–109} The magnitudes of the values measured on thin films and nanoparticles are, however, in excellent agreement. Furthermore, for thin gold films it was shown that the noninstantaneous thermalization of the initially created non-Fermi electron distribution by electron–electron scattering can be detected using low-power femtosecond pulses.^{98,104,108} It was first thought that the internal electron thermalization (electron–electron relaxation) to a Fermi electron distribution is complete within the duration of the excitation pulse and, therefore, instantaneous compared to the external electron thermalization (electron–phonon relaxation).^{99,100} However, Sun et al.¹⁰⁴ reported an internal electron thermalization time of 500 fs for a 20 nm thin gold film. Using photoemission spectroscopy, Fann et al.¹⁰⁸ measured a value of 730 fs, which can be as long as 1 ps when the excitation power of the pump pulse is lowered. This observed power dependence is opposite the one described for the electron–phonon relaxation and is explained by the fact that for higher induced electron temperatures the number of empty electronic states at the Fermi level is drastically increased.¹⁰⁸ Since the electron–electron scattering rate is determined by the number of available unoccupied states, which serve as the final states for the electron–electron scattering processes, the e^-e^- scattering rate $1/\tau_{e-e}$ is inversely proportional to the energy above the Fermi level. According to

Fermi liquid theory for electrons with an initial energy E close to the Fermi energy E_F ,¹¹⁴

$$\frac{1}{\tau_{e-e}} \propto (E - E_F)^2 \quad (12)$$

The electron–electron scattering time for a single scattering process is usually on the order of 10 fs (depending on the initial energy E). The sum of all the electron–electron scattering events that occur until a Fermi electron distribution is reached determines the internal electron thermalization, which is on the order of several hundred femtoseconds, as measured in the thin metal films. Since the external electron thermalization by electron–phonon interactions occurs on a comparable time scale, a clear separation between electron–electron and electron–phonon relaxation as sequential processes is therefore incorrect.^{98,104,108} The nonthermal electrons already interact with the phonon bath, losing their energy and thus heating the lattice, while the non-Fermi electron distribution is decaying by electron–electron scattering.¹⁰⁴

When the excitation wavelength is tuned away from the threshold for interband transitions, it is possible to detect an internal electron thermalization time for gold nanoparticles.⁷⁸ This is illustrated in Figure 9a where the plasmon bleach recovery probed at 530 nm for 22 nm particles after low power excitation is shown. The excitation wavelength was 800 nm, and only the electrons within the conduction band are excited (intraband transitions), since the interband threshold lies at about 2.4 eV in gold,¹¹⁵ corresponding to roughly 520 nm. The dotted line in Figure 9a is an exponential fit to the experimental data points and clearly cannot reproduce the observed plasmon bleach decay within the first 2 ps. During this time a slower decay is actually observed. A similar deviation from an exponential decay was not found when the excitation wavelength was 400 nm.⁷⁸ In this case, interband excitations lead to a greater perturbation of the electron gas, with electron energies far above the Fermi energy, and therefore to a faster internal electron thermalization.⁷⁸ The solid line in Figure 9a was obtained by fitting the data to a rate equation derived by Sun et al.¹⁰⁴ for their studies on gold films:

$$\Delta A(h\nu) = [\Delta A(h\nu)]_{NT} \exp\left(-\frac{t}{\tau'_{th}}\right) + [\Delta A(h\nu)]_{Th} \exp\left(-\frac{t}{\tau_{e-ph}}\right) \left\{1 - \exp\left(-\frac{t}{\tau_{th}}\right)\right\} \quad (13)$$

with

$$\frac{1}{\tau'_{th}} = \frac{1}{\tau_{th}} + \frac{1}{\tau_{e-ph}}$$

$\Delta A(h\nu)$ is the change in absorbance as a function of photon energy $h\nu$ with the subscripts NT and Th standing for nonthermal and thermalized, respectively. The temperature of the thermalized distribution decays because of electron–phonon interactions with the time constant τ_{e-ph} , and τ_{th} is the internal electron thermalization time. Note that the rise time of the thermalized distribution τ_{th} is longer than the decay time of the nonthermal population τ'_{th} , reflecting the fact that the nonthermalized electron distribution interacts with the lattice during the thermalization process.

By use of eq 13 to fit the experimental data, excellent agreement with the experimental decay curve is obtained, as seen in Figure 9a. The solid line corresponds to an internal electron thermalization time of 500 fs and an electron–phonon

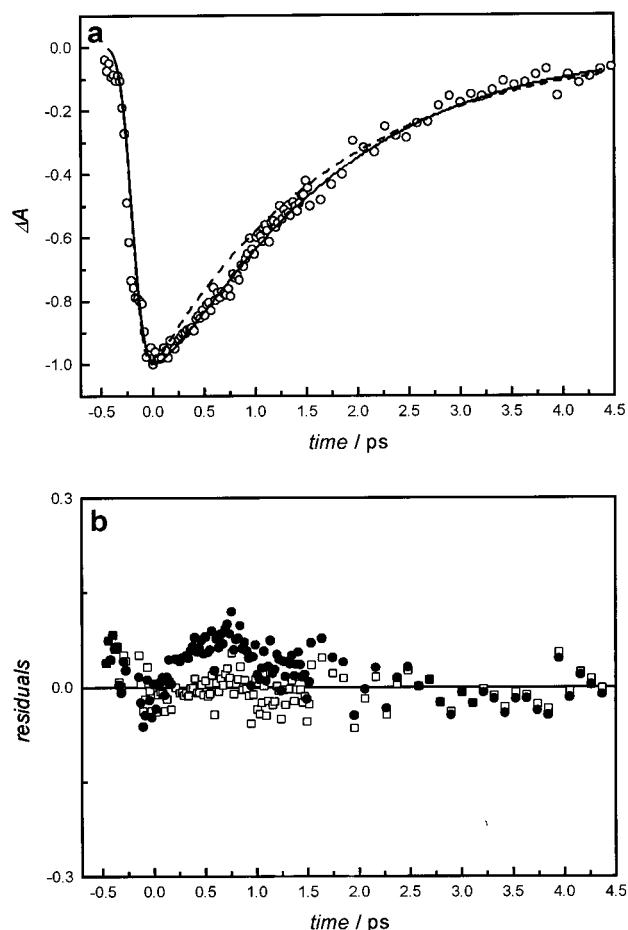


Figure 9. Importance of electron–electron thermalization in gold nanoparticles. Part a shows the plasmon bleach recovery of 22 nm gold nanoparticles probed at 530 nm after excitation at 800 nm with low-power femtosecond laser pulses. The solid line is a fit with eq 13, yielding an internal electron thermalization time of 500 fs and an electron–phonon relaxation time of 1.6 ps. A monoexponential decay (dashed line) clearly cannot describe the experimental data for the early part of the transient signal. This is also illustrated in part b where the residuals for the two fitting curves are plotted (closed circles, monoexponential fit; open squares, fit with eq 13).

relaxation time of 1.6 ps. That a fit with eq 13 indeed describes the plasmon bleach recovery better than a simple exponential decay function is further illustrated in Figure 9b where the residuals of the two fits from Figure 9a are plotted. An internal electron thermalization time of 500 fs for 22 nm gold nanoparticles also agrees well with the results obtained on bulk films^{98,104,108} and on copper nanoparticles.⁸⁵ Specifically, Bigot et al.⁸⁵ found the electron thermalization time and electron–phonon relaxation times on the order of about 1 ps for both processes measured on 10 nm particles embedded in a glass matrix.

The transient absorption spectrum of spherical gold nanoparticles has successfully been modeled by relating the changes in the differential transmittance $\Delta T/T$ to the changes in the real and imaginary parts of the dielectric function $\Delta\epsilon_1$ and $\Delta\epsilon_2$ induced by the exciting laser pulse.^{77,78,84,104}

$$\frac{\Delta T}{T} = \frac{\delta \ln T}{\delta \epsilon_1} \Delta\epsilon_1 + \frac{\delta \ln T}{\delta \epsilon_2} \Delta\epsilon_2 \quad (14)$$

The transmittance T is defined as the ratio of the transmitted to the incident light intensities, and the absorbance A (see eq 1) is the negative logarithm of the transmittance. $\Delta\epsilon_2$ is related to

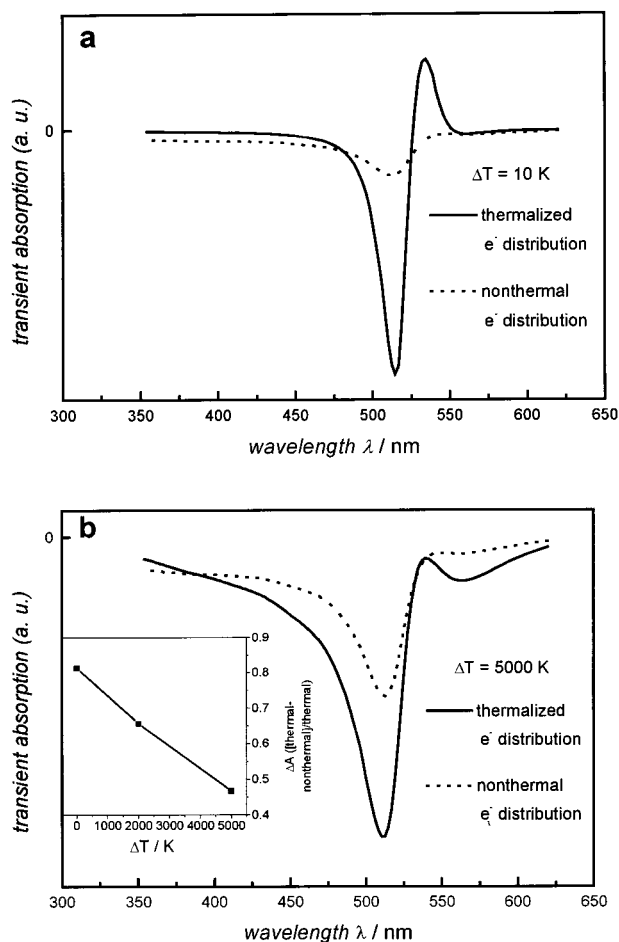


Figure 10. Calculated transient absorption spectra of gold nanoparticles for a thermalized (solid line) and nonthermal (dotted line) electron distribution. The temperature change of the electron gas is (a) 10 K and (b) 5000 K. For the non-Fermi electron distribution, excitation with photons of 2 eV energy is assumed. The bleach of the surface plasmon absorption is clearly reproduced. While the spectral shape of the transient absorption signal arising from a thermalized and nonthermal electron distribution is similar, the intensity is lower for a nonthermal distribution. Furthermore, the relative difference of the calculated transient absorption intensity originating from a nonthermal electron distribution compared to a thermalized electron gas decreases with increasing electron temperature change ΔT corresponding to higher pump powers (see inset of part b).

the occupancy of the electronic states for a certain electron distribution after photoexcitation and can be obtained following a simple approach taken by Rosei et al.^{116,117} $\Delta\epsilon_1$ is then calculated by Kramers–Kronig analysis.^{26,27}

The results from these simulations for gold nanoparticles are displayed in Figure 10. The bleach of the plasmon absorption is clearly reproduced. The solid lines in Figure 10 are obtained assuming a thermalized (Fermi) electron distribution with a temperature change ΔT of 10 and 5000 K. A comparison between parts a and b of Figure 10 shows that the line width of the bleach is much broader for a larger change in the electron temperature corresponding to a broader electron distribution and in agreement with the experimental results shown in Figure 7. The intensity of the bleach also increases with higher electron temperatures, which is not apparent from Figure 10 (see ref 78).

The dotted lines in Figure 10 were calculated with a nonthermal electron distribution corresponding to the same changes in the electron temperature of 10 and 5000 K. The intensity of the calculated plasmon bleach is considerably smaller for a non-Fermi electron distribution, which was also

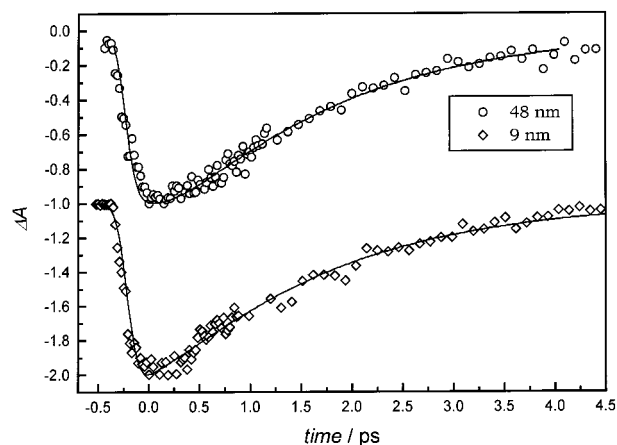


Figure 11. Size dependence of the electron–electron and electron–phonon relaxation times for spherical gold nanoparticles. The plasmon bleach recovery is probed for 9 nm (diamonds) and 48 nm (circles) gold particles at 530 nm after excitation with 630 nm femtosecond pulses. The fits give decay times of 500 and 450 fs for the internal electron thermalization (electron–electron interactions) and 1.6 and 1.7 ps for the external electron thermalization (electron–phonon interactions) for the 9 and 48 nm particles, respectively. This indicates the absence of a size dependence of the electron–electron and electron–phonon relaxation times in the size range where electron–surface scattering increases because of the limitation of the mean free path of the conduction electrons.

found for studies on gold films by Sun et al.¹⁰⁴ Furthermore, these results predict a rise time of the transient absorption signal as the initial electron distribution thermalizes to a Fermi distribution.⁷⁸ Indeed, this confirms the conclusions made for the experimental data in Figure 9a.

It is important to note that the difference in bleach intensities for a thermalized and nonthermal electron distribution decreases when the temperature change ΔT induced by the heating laser pulse increases. At high pump powers the effect of a nonthermal electron distribution on the transient absorption should be washed out. This is again in agreement with the above discussion and is further illustrated in the inset of Figure 10b, where the normalized difference between the change in absorbance for a thermalized and nonthermal electron distribution is plotted as a function of ΔT and hence pump power. The electron–electron thermalization time in metallic nanoparticles is therefore best detectable in the low excitation limit.⁷⁸

3.4. Size Dependence of the Electron–Phonon Relaxation Dynamics. In section 2.1 it was shown how the plasmon bandwidth and therefore the dephasing time T_2 depend on the nanoparticle size. The same arguments used in the model of the limitation of the electron mean free path can also be applied to the energy relaxation of the hot electron gas. In nanoparticles smaller than the mean free path an enhanced electron–surface scattering should lead to a faster electron–phonon relaxation (T_1) if the collisions of the electrons and the surface are inelastic. With the mean free path of the conduction electrons in gold being about 50 nm,^{26,27} the samples shown in Figure 1 would be ideally suited to test this hypothesis. The results of this experiment for 9 and 48 nm gold nanoparticles, in which the excitation and monitoring wavelengths were 630 and 530 nm, respectively, are given in Figure 11. The kinetic decay traces for the 9 and 48 nm particles were fitted with lifetimes of 500 and 450 fs for the internal electron thermalization (electron–electron interactions) and 1.6 and 1.7 ps for the external electron thermalization (electron–phonon interactions), respectively. It can be concluded that no size dependence of the electron–electron and electron–phonon relaxations exists in gold nano-

particles between 9 and 48 nm.⁷⁸ It should be added that the pump power was decreased until no further decrease in the measured lifetimes was observable for the 9 and 48 nm gold nanoparticles. Furthermore, the pump power and optical density of the two samples were about equal so that the change in the electronic temperature is also very similar in both systems.⁷⁸ This suggests that the surface cannot be of major importance for the energy relaxation process (T_1) of hot electrons.

One explanation for the size independence of T_1 could be that electron–surface scattering is elastic and does not lead to a transfer of energy from the hot electrons to the surface phonons. It could also be speculated that there is less effective coupling of the electrons to the surface phonons. A third possibility is based on results from HRTEM studies on 15 and 48 nm gold nanoparticles.⁷⁸ The TEM investigations verify the presence of defect structures within the gold nanoparticles. Twin boundaries and stacking faults are the dominant features.^{118–121} Those defects are present in the 9 nm as well as in the larger 48 nm gold nanoparticles. If energy relaxation by electron–defect scattering is as effective as electron–surface interactions,¹²² a possible size (surface) effect is washed out because of the existence of a broad distribution of grain sizes that are smaller than any nanoparticle size. In agreement with this explanation would be measurements on single and polycrystalline gold films in which a faster electron–phonon relaxation was found for the polycrystalline film.^{105,107}

Ahmadi et al.⁷⁷ also observed no size dependence of the electron–phonon relaxation for 1.9, 2.6, and 3.2 nm thiol-passivated gold nanocrystals compared to the measured relaxation dynamics for 30 nm colloidal gold nanoparticles prepared by the citrate method. The spectral changes in the transient absorption signal were attributed to a lower density of electronic states in the very small molecular-like nanoparticles. In agreement with these results on gold nanoparticles, Hodak et al.⁸⁴ found no change in the electron dynamics measured in 10 and in 50 nm silver particles (mean free path of the conduction electrons in silver is ~ 40 nm^{26,27}). On the other hand, Del Fatti et al.⁹¹ reported a decrease in the electron–phonon relaxation times from 800 to 500 fs for silver nanoparticles in a glass matrix as the size is reduced from 30 nm to below 8 nm. This was attributed to an increased probability of electron–surface scattering in these small particles. Also, Stella et al.^{123,124} reported a size-dependent electron–surface interaction for 2, 4, and 6 nm tin particles embedded in an Al_2O_3 matrix by femtosecond transient reflectivity measurements. They measured decreasing lifetimes with decreasing size, corresponding to an increase in electron–surface scattering in the tin nanoparticles where the mean free path is 4.4 nm. On the other hand, quantum size effects have not been discussed as a possible explanation for their results, even though the band structure could be changed in going from 2 to 6 nm tin particles. Smith et al.⁹⁰ also found a pronounced size dependence for 15 nm gold nanoparticles compared with Au_{13} and Au_{55} clusters, and also for 3 and 35 nm platinum nanoparticles. They claimed that the relaxation dynamics of the photoexcited electron gas should be described by electron–phonon coupling, which decreases with decreasing size, and electron–surface scattering, which increases with decreasing particle size. These two processes compete with each other and determine the measured lifetime. A comparison of 15 nm gold particles with very small molecular type clusters might, however, be questionable.

3.5. Shape Dependence of the Electron–Phonon Relaxation Dynamics. The next interesting question that will be addressed in this article is the effect of shape on the electron–

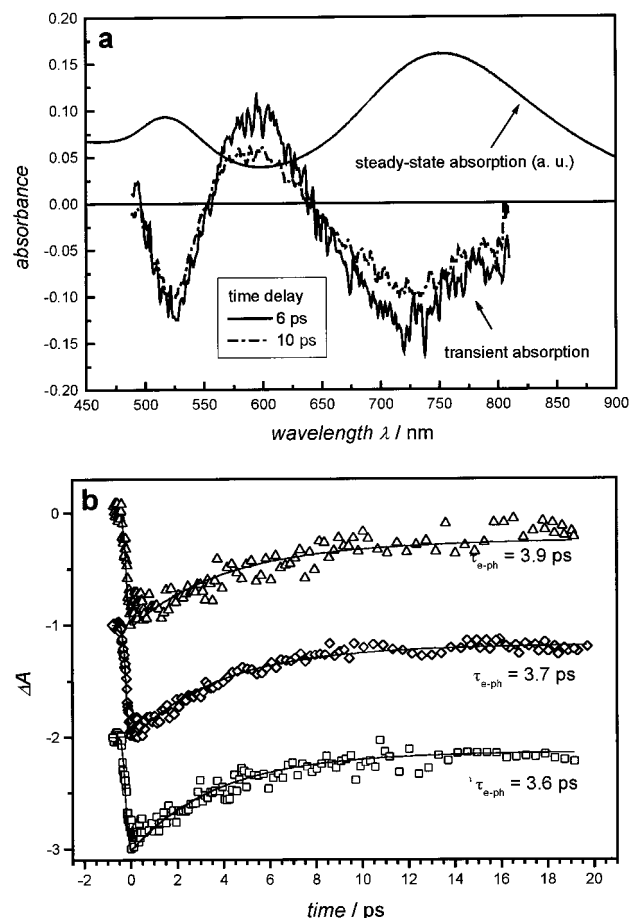


Figure 12. Shape dependence of the electron–phonon relaxation time. Part a shows the transient absorption spectra of a colloidal gold nanorod solution measured at delay times of 6 ps (solid line) and 10 ps (dotted line) after excitation with 100 fs laser pulses at 400 nm. The average aspect ratio of the gold nanorods is 3.8. The steady-state absorption spectrum is also shown for comparison. Both modes of the surface plasmon absorption are bleached after laser excitation. Part b shows the plasmon bleach recovery after excitation with 100 fs pulses at 400 nm monitored at 520 nm for the transverse surface plasmon absorption of gold nanorods with an average aspect ratio of 4.1 (triangles) and for the plasmon absorption of spherical nanoparticles prepared by chemical reduction (diamonds) and by photothermal reshaping (squares). The solid lines are fits with decay times τ_{e-ph} of 3.9, 3.7, and 3.6 ps for the electron–phonon relaxation of the three samples, respectively.

phonon relaxation dynamics.⁷⁹ As outlined in section 2.3, changing the nanoparticle shape from a sphere to a rod and, thus, introducing an anisotropy result in the splitting of the surface plasmon resonance into two modes. The effect on the femtosecond transient absorption spectrum is shown in Figure 12a for a colloidal gold nanorod solution with an average aspect ratio of 3.8. Both the transverse and the longitudinal mode of the plasmon absorption are bleached because of laser heating of the electron gas with 400 nm femtosecond pulses.⁷⁹ The two bleach features and the positive absorption around 600 nm are in agreement with the explanation given above for the transient absorption spectrum of spherical gold nanoparticles. The spectral features result from the broadening of the transverse and longitudinal plasmon bands after photoexcitation. The spectra in Figure 12a also suggest that the magnitude of the transient bleach is less pronounced for the longitudinal plasmon band than for the transverse, especially when the intensities of those two bands in the steady-state absorption spectrum are compared (see Figure 12a). This last observation could, however, be

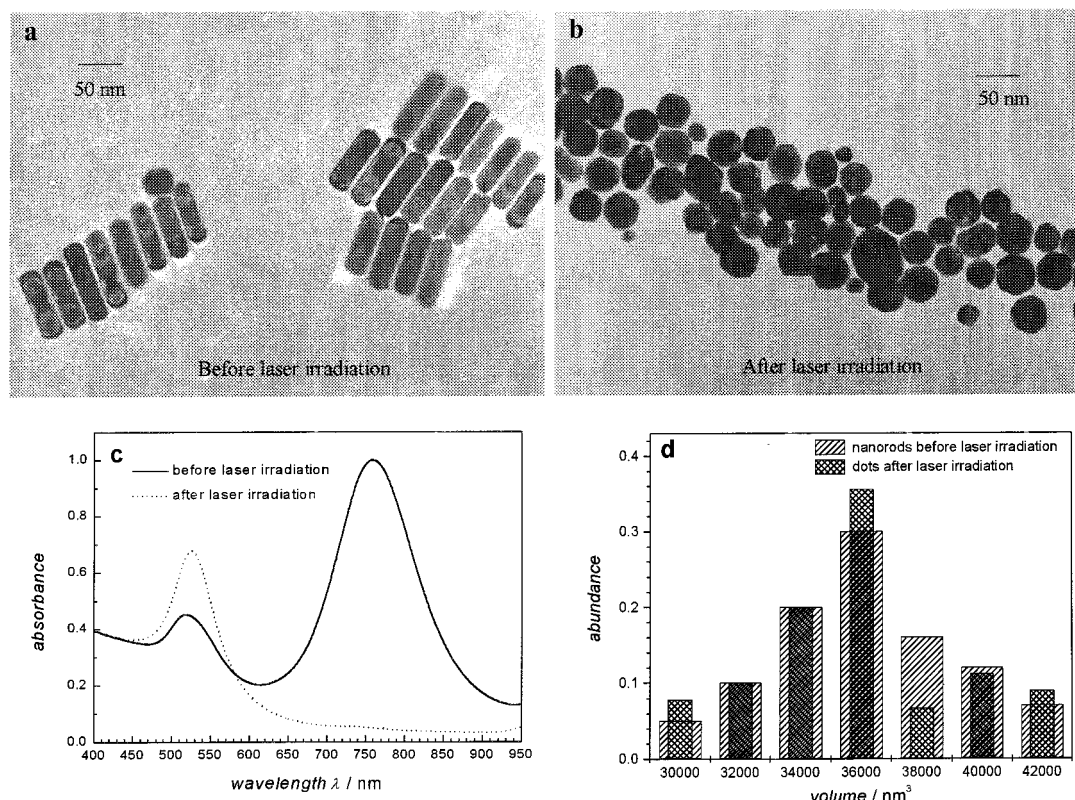


Figure 13. Effect of laser heating on gold nanorods, shown in TEM images of a colloidal gold nanorod solution having a mean aspect ratio 3.8 before (a) and after (b) irradiation with 100 fs laser pulses centered at 800 nm. The pulse energy was 52 μJ . A shape transformation from nanorods to spherical nanoparticles has taken place. The corresponding UV-vis absorption spectra of this colloidal gold solution before (solid line) and after (dotted line) irradiation with 100 fs laser pulses is given in part c. The longitudinal plasmon absorption band disappeared in accordance with the shape transformation seen in the TEM images. The volume of the gold nanorods before laser irradiation is compared to the volume of the spheres produced by this photothermal reshaping in part d. This result therefore suggests that the nanorods melt because of laser heating and then transform into the more stable spherical shape.

somewhat obscured by the photothermal instability of the gold nanorods (see section 3.6 below).^{79,125}

The electron-phonon relaxation time measured for the same gold nanorod solution as shown in Figure 12a was found to be 2.9 and 3.1 ps when monitored at 520 nm (transverse mode) and 700 nm (longitudinal mode), respectively.⁷⁹ Thus, the change in the nanoparticle shape (facets) and type of surface plasmon oscillation do not have an effect on the electron-phonon dynamics. A further proof of the shape and size independence of the electron-phonon relaxation of gold nanoparticles is given in Figure 12b. The plasmon bleach recovery at 520 nm was probed for gold nanorods having a mean aspect ratio of 4.1 (triangles), 15 nm spherical gold nanoparticles prepared by chemical reduction (diamonds), and 17 nm spheres obtained by photothermal reshaping¹²⁵ of the gold nanorods (squares). Fits to the kinetic traces in Figure 12b give nearly identical decay times of 3.9, 3.7, and 3.6 ps. The optical density of the three solutions was adjusted to the same value at the excitation wavelength of 400 nm, and the same pump power was used in this experiment, which allows a direct comparison of the electron-phonon relaxation times.⁷⁹ The independence of the electron-phonon relaxation rates on the types of surface facets (i.e., particle shape) or electron surface oscillation (i.e., transverse vs longitudinal) strongly suggests that the electron-phonon energy relaxation T_1 of the hot electrons in gold nanoparticles does not involve electron-surface scattering. In addition, the independence of the relaxation time on the preparation method (chemical reduction vs photothermal reshaping) suggests that electron-defect scattering as mentioned in section 3.4 can only be of minor importance.

3.6. Photothermal Stability of Gold Nanorods. An interesting nanoparticle shape transformation is observed when the colloidal gold nanorod solutions are exposed to femtosecond laser pulses.¹²⁵ A TEM image of gold nanorods with an average aspect ratio of 3.8 is shown in Figure 13a. Figure 13b displays an image of the same gold nanorod solution taken after exposure to 100 fs laser pulses with a pulse energy of 52 μJ and an estimated laser spot diameter of roughly 100 μm . The wavelength of the exciting laser light was 800 nm in this experiment and coincides with the absorption of the longitudinal plasmon absorption. From Figure 13b it is clear that all the gold nanorods transformed into spheres after exposure to the femtosecond laser pulses. The disappearance of the longitudinal plasmon band in the UV-vis absorption spectrum (Figure 13c) is in agreement with the TEM results. Figure 13c further demonstrates that the transverse mode of the plasmon absorption of gold nanorods is less intense than the surface plasmon absorption of spherical gold nanoparticles.¹²⁵ Since the volume of the spherical particles produced is comparable to that of the nanorods before exposure to laser light (Figure 13d), the intense photothermal heating with the high power femtosecond laser pulses must melt the gold nanorods into spheres.

More detailed studies of this system have proven that the observed shape transformation of colloidal gold nanorods is not only energy-dependent but also laser-pulse-width-dependent.¹²⁵ Lowering the pulse energy of the femtosecond pulses (below 1 μJ but strongly dependent on the spot size of the laser beam) leads to a hole burning within the absorption cross section of the longitudinal surface plasmon resonance (Figure 14a), since only the nanorods that absorb strongly at the laser wavelength

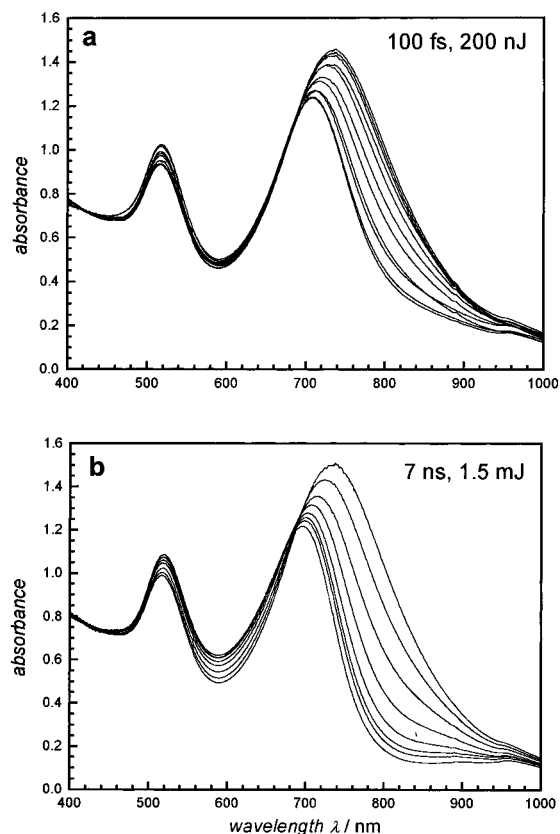


Figure 14. Low-power laser reshaping of gold nanorods and the effect of laser pulse-width. UV-vis absorption spectra of gold nanorods recorded after different exposure times to (a) 200 nJ femtosecond and (b) 1.5 mJ nanosecond laser pulses are shown. The wavelength of the two lasers was tuned to 800 nm where the longitudinal plasmon resonance of the gold nanorods absorbs. This optical hole burning is only observed at low pulse energies and effectively narrows the size distribution by transforming the longest nanorods into shorter rods or spheres. Note that the pulse energy of the nanosecond laser in part b is higher than the energy of the femtosecond laser used in the experiment shown in Figure 13 (1.5 mJ compared to 52 μ J), which leads to the conclusion that the observed laser-induced shape changes in gold nanorods are not only energy-dependent but also laser-pulse-width-dependent.

are heated enough to transform into spherical particles. When the wavelength of the femtosecond laser is tuned to the red edge of the longitudinal plasmon absorption, a narrowing of the inhomogeneous gold nanorod size distribution can easily be achieved¹²⁵ (see Figure 14a), which is otherwise impossible by size-selective precipitation methods for these gold nanorods encapsulated by micelles. A shape transformation into shorter and wider nanorods is also observed, consistent with a laser-induced premelting or surface melting of the rods. The melting point depression for nanoparticles has been extensively studied; it is caused by the high surface tension of these nanoparticles.^{126–132} That melting starts on the surface of materials is in fact also well-known. Recently, an in situ TEM study on cubic, tetrahedral, and other shape platinum nanoparticles showed the lowering of the melting temperature from a bulk value of 1770 °C to only \sim 600 °C.¹³³

Results similar to those obtained with the low-energy femtosecond pulses are also seen when the exciting light source is a nanosecond laser tuned to the same wavelength.¹²⁵ However, the nanosecond pulse energy is higher than the femtosecond one, which led to the complete melting of the gold nanorods (Figure 13c). This is illustrated in Figure 14 where the effects on the optical absorption spectrum of gold nanorods caused by

200 nJ femtosecond (a) and 1.5 mJ (!) nanosecond (b) laser pulses are compared. An increase of the pulse energy to 20 mJ leads to the fragmentation of the gold nanorods into smaller, near-spherical particles by the nanosecond laser pulses. This difference in energy and laser pulse width can be explained in terms of the rates of energy deposition compared to the electron-phonon and phonon-phonon relaxation processes responsible for the cooling of the gold nanorods. The heating of the gold nanorods by the selective excitation of the conduction electrons and subsequent thermal equilibration with the lattice by electron-phonon collisions occur in the dark with the femtosecond laser, since the electron-phonon relaxation time is a few picoseconds^{76–78} (see sections 3.1, 3.2, and 3.5). Within the pulse duration of the nanosecond laser the gold particles constantly absorb additional photons while the lattice is already hot, which leads to an increase in the lattice internal energy. This then results in the fragmentation of the gold nanorods, since the heat transfer to the surrounding medium is slow (on the order of 100 ps).^{76–78}

The melting of gold nanorods induced by a nanosecond laser was also reported by Chang et al.¹³⁴ Irradiation of gold nanorod solutions with 532 nm laser light and therefore exciting the transverse plasmon absorption resulted in a rod-to-sphere conversion, while excitation of the longitudinal plasmon absorption at 1064 nm induced only an incomplete photoannealing process leading to ϕ -shaped particles and bent and twisted nanostructures. The authors suggest¹³⁴ that these new shapes represent an early stage of the shape transformation from the rods to the spheres and that the restructuring of the gold nanorods starts from the center portion of the particle.

Laser-induced fragmentation has also been observed for spherical gold nanoparticles in solution.^{135,136} The gold nanoparticles in this study were irradiated with 532 nm nanosecond pulses, and the slow heat transfer to the surrounding medium in combination with the intense heating of the gold lattice was thought to be responsible for the observed fragmentation of the gold nanoparticles.^{135,136} This explanation is similar to the one described above. On the other hand, photofragmentation of spherical silver clusters with diameters of 40–60 nm upon irradiation with 355 nm picosecond pulses has been reported by Kamat et al.¹³⁷ They propose in their model the ejection of electrons due to multiphoton ionization, which then leads to the charging of the nanoparticles. The repulsion of the accumulated charges within the nanoparticles leads to fragmentation into smaller clusters.

Acknowledgment. This work was supported by the National Science Foundation (Grant No. CHE 9705164) and the Office of Naval Research (Contract No. N00014-95-1-0306).

References and Notes

- (1) Henglein, A. *J. Phys. Chem.* **1993**, 97, 8457.
- (2) Henglein, A. *Chem. Rev.* **1989**, 89, 1861.
- (3) Alivisatos, A. P. *J. Phys. Chem.* **1996**, 100, 13226.
- (4) Schmid, G. *Clusters and Colloids: From Theory to Application*; VCH: Weinheim, 1994.
- (5) Perenboom, J. A. A. J.; Wyder, P.; Meier, P. *Phys. Rep.* **1981**, 78, 173.
- (6) Hughes, A. E.; Jain, S. C.; *Adv. Phys.* **1979**, 28, 717.
- (7) Kamat, P. V.; Meisel, D. *Semiconductor Nanoclusters—Physical, Chemical, and Catalytic Aspects*; Kamat, P. V., Meisel, D., Eds.; Studies in Surface Science and Catalysis 103; Elsevier: Amsterdam, 1997.
- (8) Brus, L. E. *J. Chem. Phys.* **1983**, 79, 5566.
- (9) Brus, L. E. *J. Chem. Phys.* **1984**, 80, 4403.
- (10) Brus, L. E. *Appl. Phys. A* **1991**, 53, 465.
- (11) Edelstein, A. S.; Cammarata, R. C. *Nanoparticles: Synthesis, Properties and Applications*; Institute of Physics Publishing: Bristol, 1996.

- (12) Graetzel, M. In *Electrochemistry in Colloids and Dispersions*; Mackay, R. A., Texter, J., Eds.; VCH: Weinheim, 1992.
- (13) Kerker, M. *J. Colloid Interface Sci.* **1985**, *105*, 297.
- (14) Faraday, M. *Philos. Trans.* **1857**, *147*, 145.
- (15) Mie, G. *Ann. Phys.* **1908**, *25*, 377.
- (16) Papavassiliou, G. C. *Prog. Solid State Chem.* **1980**, *12*, 185.
- (17) Kerker, M. *The Scattering of Light and Other Electromagnetic Radiation*; Academic Press: New York, 1969.
- (18) Bohren, C. F.; Huffman, D. R. *Absorption and Scattering of Light by Small Particles*; Wiley: New York, 1983.
- (19) Creighton, J. A.; Eadon, D. G. *J. Chem. Soc., Faraday Trans.* **1991**, *87*, 3881.
- (20) Mulvaney, P. *Langmuir* **1996**, *12*, 788.
- (21) Kreibig, U.; Vollmer, M. *Optical Properties of Metal Clusters*; Springer: Berlin, 1995.
- (22) Kreibig, U.; v. Fragstein, C. *Z. Phys.* **1969**, *224*, 307.
- (23) Kreibig, U. *Z. Phys.* **1970**, *234*, 307.
- (24) Kreibig, U.; Genzel, U. *Surf. Sci.* **1985**, *156*, 678.
- (25) Alvarez, M. M.; Khoury, J. T.; Schaaff, T. G.; Shafigullin, M. N.; Vezmer, I.; Whetten, R. L. *J. Phys. Chem. B* **1997**, *101*, 3706.
- (26) Ashcroft, N. W.; Mermin, N. D. *Solid State Physics*; Saunders College: Philadelphia, 1976.
- (27) Kittel, C. *Introduction to Solid State Physics*; Wiley: New York, 1996.
- (28) Kawabata, A.; Kubo, R. *J. Phys. Soc. Jpn.* **1966**, *21*, 1765.
- (29) Persson, N. J. *Surf. Sci.* **1993**, *281*, 153.
- (30) Yannouleas, C.; Broglia, R. A. *Ann. Phys.* **1992**, *217*, 105.
- (31) Cini, M. *J. Opt. Soc. Am.* **1981**, *71*, 386.
- (32) Genzel, L.; Martin, T. P.; Kreibig, U. *Z. Phys. B* **1975**, *21*, 339.
- (33) Kraus, W. A.; Schatz, G. C. *J. Chem. Phys.* **1983**, *79*, 6130.
- (34) Link, S.; El-Sayed, M. A. *J. Phys. Chem. B* **1999**, *103*, 4212.
- (35) Turkevich, J.; Stevenson, P. C.; Hillier, J. *Discuss. Faraday Soc.* **1951**, *11*, 55.
- (36) Turkevich, J.; Garton, G.; Stevenson, P. C. *J. Colloid Sci.* **1954**, *Suppl. 1*, 26.
- (37) Handley, D. A. *Colloidal Gold: Principles, Methods, and Applications*; Academic Press: New York, 1989; Vol. 1.
- (38) Turro, N. J. *Modern Molecular Photochemistry*; University Science Books: Mill Valley, CA, 1991.
- (39) Heilweil, E. J.; Hochstrasser, R. M. *J. Chem. Phys.* **1985**, *82*, 4762.
- (40) Puech, K.; Henari, F. Z.; Blau, W. J.; Duff, D.; Schmid, G. *Chem. Phys. Lett.* **1995**, *247*, 13.
- (41) Puech, K.; Henari, F. Z.; Blau, W. J.; Duff, D.; Schmid, G. *Europhys. Lett.* **1995**, *32*, 119.
- (42) Bloemer, M. J.; Haus, J. W.; Ashley, P. R. *J. Opt. Soc. Am. B* **1990**, *7*, 790.
- (43) Puech, K.; Blau, W.; Grund, A.; Bubeck, C.; Gardenas, G. *Opt. Lett.* **1995**, *20*, 1613.
- (44) Papavassiliou, G. C. *J. Phys. F: Met. Phys.* **1976**, *6*, L103.
- (45) Sinzig, J.; Radtke, U.; Quinten, M.; Kreibig, U. *Z. Phys. D* **1993**, *26*, 242.
- (46) Teo, B. K.; Keating, K.; Kao, Y.-H. *J. Am. Chem. Soc.* **1987**, *109*, 3494.
- (47) Treguer, M.; de Cointet, C.; Remita, H.; Khatouri, J.; Mostafavi, M.; Amblard, J.; Belloni, J.; de Keyser, R. *J. Phys. Chem. B* **1998**, *102*, 4310.
- (48) Link, S.; Wang, Z. L.; El-Sayed, M. A. *J. Phys. Chem. B* **1999**, *103*, 3529.
- (49) Carey Lea, M. *Am. J. Sci.* **1889**, *37*, 476.
- (50) Mulvaney, P.; Giersig, M.; Henglein, A. *J. Phys. Chem.* **1993**, *97*, 7061.
- (51) Turkevich, J. *Gold Bull.* **1985**, *18*, 86.
- (52) Turkevich, J. *Gold Bull.* **1985**, *18*, 125.
- (53) Schwank, J. *Gold Bull.* **1983**, *16*, 98.
- (54) Schwank, J. *Gold Bull.* **1983**, *16*, 103.
- (55) Hummel, R. E. *Optische Eigenschaften von Metallen und Legierungen*; Springer: Berlin, 1971.
- (56) Johnson, P. B.; Christy, R. W. *Phys. Rev. B* **1972**, *6*, 4370.
- (57) Ripken, K. *Z. Phys.* **1972**, *250*, 228.
- (58) Linnert, T.; Mulvaney, P.; Henglein, A. *J. Phys. Chem.* **1993**, *97*, 679.
- (59) Hoevel, H.; Fritz, S.; Hilger, A.; Kreibig, U.; Vollmer, M. *Phys. Rev. B* **1993**, *48*, 18178.
- (60) Kreibig, U.; Gartz, M.; Hilger, A. *Ber. Bunsen-Ges. Phys. Chem.* **1997**, *101*, 1593.
- (61) Gans, R. *Ann. Phys.* **1915**, *47*, 270.
- (62) Yu, Y.; Chang, S.; Lee, C.; Wang, C. R. *J. Phys. Chem. B* **1997**, *101*, 34, 6661.
- (63) Mohamed, M. B.; Link, S.; El-Sayed, M. A. *J. Phys. Chem. B* **1998**, *102*, 9370.
- (64) Link, S.; Mohamed, M. B.; El-Sayed, M. A. *J. Phys. Chem. B* **1999**, *103*, 3073.
- (65) v. d. Zande, B. M. I.; Bohmer, M. R.; Fokkink, L. G. J.; Schonenberger, C. *J. Phys. Chem. B* **1997**, *101*, 852.
- (66) Foss, C. A.; Hornyak, G. L.; Tierney, M. J.; Martin, C. R. *J. Phys. Chem.* **1992**, *96*, 9001.
- (67) Hornyak, G. L.; Patrissi, C. J.; Martin, C. R. *J. Phys. Chem. B* **1997**, *101*, 1548.
- (68) Foss, C. A.; Hornyak, G. L.; Stockert, J. A.; Martin, C. R. *J. Phys. Chem.* **1992**, *96*, 7497.
- (69) Foss, C. A.; Hornyak, G. L.; Stockert, J. A.; Martin, C. R. *J. Phys. Chem.* **1994**, *98*, 2963.
- (70) Hornyak, G. L.; Martin, C. R. *Thin Solid Films* **1997**, *303*, 84.
- (71) Aspnes, D. E.; Heller, A.; Porter, J. D. *J. Appl. Phys.* **1986**, *60*, 3028.
- (72) Aspnes, D. E. *Thin Solid Films* **1982**, *89*, 249.
- (73) Kreibig, U.; Althoff, A.; Pressmann, H. *Surf. Sci.* **1981**, *106*, 308.
- (74) Quinten, M.; Kreibig, U. *Surf. Sci.* **1986**, *172*, 557.
- (75) Quinten, M.; Schoenauer, D.; Kreibig, U. *Z. Phys. D* **1989**, *26*, 239.
- (76) Ahmadi, T. S.; Logunov, S. L.; El-Sayed, M. A. *J. Phys. Chem.* **1996**, *100*, 8053.
- (77) Ahmadi, T. S.; Logunov, S. L.; El-Sayed, M. A.; Khoury, J. T.; Whetten, R. L. *J. Phys. Chem. B* **1997**, *101*, 3713.
- (78) Link, S.; Burda, C.; Wang, Z. L.; El-Sayed, M. A. *J. Chem. Phys.* **1999**, *111*, 1255.
- (79) Link, S.; Burda, C.; Mohamed, M. B.; Nikoobakht, B.; El-Sayed, M. A. *Phys. Rev. B*, submitted.
- (80) Perner, M.; Bost, P.; Pauck, T.; v. Plessen, G.; Feldmann, J.; Becker, U.; Mennig, M.; Porstendorfer, J.; Schmitt, M.; Schmidt, H. In *Ultrafast Phenomena X*; Babara, P. F., Fujimoto, J. G., Knox, W. H., Zinth, W., Eds.; Springer: Berlin, 1996.
- (81) Perner, M.; Bost, P.; v. Plessen, G.; Feldmann, J.; Becker, U.; Mennig, M.; Schmidt, H. *Phys. Rev. Lett.* **1997**, *78*, 2192.
- (82) Perner, M.; Klar, T.; Grosse, S.; Lemmer, U.; v. Plessen, G.; Spirk, W.; Feldmann, J. *J. Lumin.* **1998**, *76-77*, 181.
- (83) Hodak, J. K.; Martini, I.; Hartland, G. V. *Chem. Phys. Lett.* **1998**, *284*, 135.
- (84) Hodak, J. K.; Martini, I.; Hartland, G. V. *J. Phys. Chem. B* **1998**, *102*, 6958.
- (85) Bigot, J.-Y.; Merle, J.-C.; Cregut, O.; Daunois, A. *Phys. Rev. Lett.* **1995**, *75*, 4702.
- (86) Shahbazy, T. V.; Perakis, I. E.; Bigot, J.-Y. *Phys. Rev. Lett.* **1998**, *81*, 3120.
- (87) Roberti, T. W.; Smith, B. A.; Zhang, J. Z. *J. Chem. Phys.* **1995**, *102*, 3860.
- (88) Smith, B. A.; Waters, D. M.; Faulhaber, A. E.; Kreger, M. A.; Roberti, T. W.; Zhang, J. Z. *J. Sol-Gel Sci. Technol.* **1997**, *9*, 125.
- (89) Faulhaber, A. E.; Smith, B. A.; Andersen, J. K.; Zhang, J. Z. *Mol. Cryst. Liq. Cryst.* **1996**, *283*, 25.
- (90) Smith, B. A.; Zhang, J. Z.; Giebel, U.; Schmid, G. *Chem. Phys. Lett.* **1997**, *270*, 139.
- (91) Del Fatti, N.; Flytzanis, C.; Vallee, F. *Appl. Phys. B* **1999**, *68*, 433.
- (92) Feldstein, M. J.; Keating, C. D.; Liao, Y.-H.; Natan, M. J.; Scherer, N. F. *J. Am. Chem. Soc.* **1997**, *119*, 6638.
- (93) Inouye, H.; Tanaka, K.; Tanahashi, I.; Hirao, K. *Phys. Rev. B* **1998**, *57*, 11334.
- (94) Tokizaki, T.; Nakamura, A.; Kaneko, S.; Uchida, K.; Omi, S.; Tanji, H.; Asahara, Y. *Appl. Phys. Lett.* **1994**, *65*, 941.
- (95) Averitt, R. D.; Westcott, S. L.; Halas, N. J. *Phys. Rev. B* **1998**, *58*, 10203.
- (96) Anisimov, L.; Kapeliovich, B. L. T. L. *Perel'man, Sov. Phys. JETP* **1975**, *39*, 375.
- (97) Groeneveld, R. H. M.; Sprik, R.; Lagendijk, A. *Phys. Rev. B* **1992**, *45*, 5079.
- (98) Groeneveld, R. H. M.; Sprik, R.; Lagendijk, A. *Phys. Rev. B* **1995**, *51*, 11433.
- (99) Esley, G. L. *Phys. Rev. Lett.* **1983**, *51*, 2140.
- (100) Esley, G. L. *Phys. Rev. B* **1986**, *33*, 2144.
- (101) Schoenlein, R. W.; Lin, W. Z.; Fujimoto, J. G.; Esley, G. L. *Phys. Rev. Lett.* **1987**, *58*, 1680.
- (102) Brorson, S. D.; Fujimoto, J. G.; Ippen, E. P. *Phys. Rev. Lett.* **1987**, *59*, 1962.
- (103) Sun, C.-K.; Vallee, F.; Acioli, L. H.; Ippen, E. P.; Fujimoto, J. G. *Phys. Rev. B* **1993**, *48*, 12365.
- (104) Sun, C.-K.; Vallee, F.; Acioli, L. H.; Ippen, E. P.; Fujimoto, J. G. *Phys. Rev. B* **1994**, *50*, 15337.
- (105) Elsayed-Ali, H. E.; Juhasz, T.; Smith, G. O.; Bron, W. E. *Phys. Rev. B* **1991**, *43*, 4488.
- (106) Juhasz, T.; Elsayed-Ali, H. E.; Hu, H.; Bron, W. E. *Phys. Rev. B* **1992**, *45*, 13819.
- (107) Juhasz, T.; Elsayed-Ali, H. E.; Smith, G. O.; Suarez, C.; Bron, W. E. *Phys. Rev. B* **1993**, *48*, 15488.
- (108) Fann, W. S.; Storz, R.; Tom, H. W. K.; Boker, J. *Phys. Rev. B* **1992**, *46*, 13592.

- (109) Fann, W. S.; Storz, R.; Tom, H. W. K.; Boker, J. *Phys. Rev. Lett.* **1992**, *68*, 2834.
- (110) Schmittenmaer, C. A.; Aeschlimann, M.; Elsayed-Ali, H. E.; Miller, R. J. D.; Mantell, D. A.; Cao, J.; Gao, Y. *Phys. Rev. B* **1994**, *50*, 8957.
- (111) Aeschlimann, M.; Schmittenmaer, C. A.; Elsayed-Ali, H. E.; Miller, R. J. D.; Cao, J.; Gao, Y.; Mantell, D. A. *J. Chem. Phys.* **1995**, *102*, 8606.
- (112) Gao, Y.; Cao, J.; Miller, R. J. D.; Elsayed-Ali, H. E.; Mantell, D. A. *Phys. Rev. B* **1997**, *56*, 1099.
- (113) Cao, J.; Gao, Y.; Elsayed-Ali, H. E.; Miller, R. J. D.; Mantell, D. A. *Phys. Rev. B* **1998**, *58*, 10948.
- (114) Pines, D.; Nozieres, P. *The Theory of Quantum Liquids*; Benjamin: New York, 1966.
- (115) Christensen, N. E.; Seraphin, B. O. *Phys. Rev. B* **1971**, *4*, 3321.
- (116) Rosei, R.; Antongeli, F.; Grassano, U. M. *Surf. Sci.* **1973**, *37*, 689.
- (117) Cardona, M. In *Modulation Spectroscopy, Solid State Physics Supplement II*; Seitz, F., Turnbull, D., Ehrenreich, H., Eds.; Academic Press: New York, 1969.
- (118) Wang, Z. L. *Adv. Mater.* **1998**, *10*, 13.
- (119) Buffat, P.-A.; Flueeli, M.; Spycher, R.; Stadelmann, P.; Borel, J.-P. *Faraday Discuss.* **1991**, *92*, 173.
- (120) Smith, D. J.; Marks, L. D. *J. Cryst. Growth* **1981**, *54*, 433.
- (121) Smith, D. J.; Marks, L. D. *J. Cryst. Growth* **1981**, *54*, 425.
- (122) Wang, Z. L. *Elastic and Inelastic Scattering in Electron Diffraction and Imaging*; Plenum Press: New York, 1995.
- (123) Stella, A.; Nisoli, M.; De Silvestri, S.; Svelto, O.; Lanzani, G.; Cheyssac, P.; Kofman, R. *Phys. Rev. B* **1996**, *53*, 15497.
- (124) Stella, A.; Nisoli, M.; De Silvestri, S.; Svelto, O.; Lanzani, G.; Cheyssac, P.; Kofman, R. In *Ultrafast Phenomena X*; Babara, P. F., Fujimoto, J. G., Knox, W. H., Zinth, W., Eds.; Springer: Berlin, 1996.
- (125) Link, S.; Burda, C.; Mohamed, M. B.; Nikoobakht, B.; El-Sayed, M. A. *J. Phys. Chem. A* **1999**, *103*, 1165.
- (126) Schmidt, M.; Kusche, R.; v. Issendorff, B.; Haberland, H. *Nature* **1998**, *393*, 238.
- (127) Lewis, L. J.; Jensen, P.; Barrat, J.-L. *Phys. Rev. B* **1997**, *56*, 2248.
- (128) Ercoles, F.; Andreoni, W.; Tosattie, E. *Phys. Rev. Lett.* **1991**, *66*, 911.
- (129) Shi, F. G. *J. Mater. Res.* **1994**, *9*, 1307.
- (130) Iijima, S.; Ichihashi, T. *Phys. Rev. Lett.* **1996**, *56*, 616.
- (131) Smith, D. J.; Petford-Long, A. K.; Wallenberg, L. R.; Bovin, J.-O. *Science* **1996**, *233*, 872.
- (132) Buffat, P.; Borel, J.-P. *Phys. Rev. A* **1976**, *13*, 2287.
- (133) Wang, Z. L.; Petroski, J. M.; Green, T. C.; El-Sayed, M. A. *J. Phys. Chem. B* **1998**, *102*, 6145.
- (134) Chang, S.; Shih, C.; Chen, C.; Lai, W.; Wang, C. R. C. *Langmuir* **1999**, *15*, 701.
- (135) Kurita, H.; Takami, A.; Koda, S. *Appl. Phys. Lett.* **1998**, *72*, 789.
- (136) Takami, A.; Kurita, H.; Koda, S. *J. Phys. Chem. B* **1999**, *103*, 1226.
- (137) Kamat, P. V.; Flumiani, M.; Hartland, G. V. *J. Phys. Chem. B* **1998**, *102*, 3123.